Graduate School ETD Form 9
(Revised 12/07)

PURDUE UNIVERSITY
GRADUATE SCHOOL
Thesis/Dissertation Acceptance

This is to certify that the thesis/dissertation prepared

By QI LIU

Entitled SYNTHESIS OF MESOPOROUS PHOSPHATES VIA SOLID STATE REACTION AT LOW TEMPERATURE

For the degree of MASTER OF SCIENCE IN MECHANICAL ENGINEERING

Is approved by the final examining committee:

Chair	
JIAN XIE	
RUIHUA CHENG	
LIKUN ZHU	

To the best of my knowledge and as understood by the student in the *Research Integrity and Copyright Disclaimer (Graduate School Form 20)*, this thesis/dissertation adheres to the provisions of Purdue University's "Policy on Integrity in Research" and the use of copyrighted material.

Approved by Major Professor(s): JIAN XIE

Approved by: JIE CHEN 07/19/2010
Head of the Graduate Program Date

Graduate School Form 20
(Revised 1/10)

PURDUE UNIVERSITY
GRADUATE SCHOOL

Research Integrity and Copyright Disclaimer

Title of Thesis/Dissertation:
SYNTHESIS OF MESOPOROUS PHOSPHATES VIA SOLID STATE REACTION AT LOW TEMPERATURE

For the degree of MASTER OF SCIENCE IN MECHANICAL ENGINEERING

I certify that in the preparation of this thesis, I have observed the provisions of *Purdue University Teaching, Research, and Outreach Policy on Research Misconduct (VIII.3.1)*, October 1, 2008.*

Further, I certify that this work is free of plagiarism and all materials appearing in this thesis/dissertation have been properly quoted and attributed.

I certify that all copyrighted material incorporated into this thesis/dissertation is in compliance with the United States' copyright law and that I have received written permission from the copyright owners for my use of their work, which is beyond the scope of the law. I agree to indemnify and save harmless Purdue University from any and all claims that may be asserted or that may arise from any copyright violation.

QI LIU
Printed Name and Signature of Candidate

07/19/2010
Date (month/day/year)

*Located at http://www.purdue.edu/policies/pages/teach_res_outreach/viii_3_1.html

SYTHESIS OF MESOPOROUS PHOSPHATES VIA SOLID STATE REACTION AT LOW TEMPERATURE

A Thesis
Submitted to the Faculty
of
Purdue University
by
Qi Liu

In Partial Fulfillment of the
Requirements for the Degree
of
Master of Science in Mechanical Engineering

August 2010
Purdue University
Indianapolis, Indiana

ACKNOWLEDEGMENTS

I would like to thank my advisor, Professor Jian Xie, for his guidance, encouragement, support, and patience during the entire course of this research and thesis work. He was always willing to get involved with the sometime troublesome experiment design if I was having trouble, and give me helpful suggestions that helped solve problems in the lab.

I would also like to thank Professor Jie Chen for his guidance and advice with this project and my graduate school life. I am grateful to Professor Ruihua Cheng for being a part of my thesis committee and for his valuable comments on my thesis.

I would like to extend my special thanks to present Dr Jian Xie's group members. Dr. Moxian Wang has taught me, in many ways, so that I can adapt to the research environment quickly and has given me great suggestions for this project. I am also in great debt to Hao He and Fan Xu for their help in the lab and brilliant comments on my thesis.

I would also like to thank Ms. Valerie Lim Diemer and Ms. Ginger Jessop Lauderback for assisting me in formatting this thesis. I am grateful for the people from the Mechanical Engineering department at PUI, My friends, Noma, Seth, Deric, Joe, Chan, Zhiyao, and many more. Without them, graduate life would have never been the same. Finally, I express my gratitude to my parents for their support and encouragement during my life.

TABLE OF CONTENTS

Page

Page

LIST OF TABLES

LIST OF FIGURES

Figure Page

ABSTRACT

Liu, Qi. Purdue University, August 2010. Synthesis of Mesoporous Phosphates Via Solid State Reaction at Low Temperature. Major Professor: Jian Xie.

Three parts consist of my thesis work centered on the synthesis of inorganic phosphates and then metal organic frame work (MOF). The first part is the synthesis of mesoporous chromium phosphates using the room temperature solid state reaction (SSR) approach. One of the major aims of this work is to fill the gap of lacking a low cost, low or zero pollution, easy method to synthesize phosphates. The room temperature solid state reaction has been demonstrated in this work is such a method. Mesoporous chromium phosphates were prepared using the solid state reaction at low temperature using $CrCl_3 \cdot 6H_2O$, and $NaH_2PO_4 \cdot 2H_2O$ as precursors and the surfactant cetyltrimethyl ammonium bromide (CTAB) as template. The synthesized chromium phosphates were characterized by XRD, EDS, HR-TEM, N_2-physisorption, TG-DSC and UV-Vis spectroscopies. The results indicate that chromium phosphate mesophases were formed only at atomic ratios of P/Cr $\geq$ 1.8. The mesophase for P/Cr = 2.0 phosphate possessed the highest ordering of pore array, with a specific surface area as high as 250.78 m^2/g and an average pore size of 3.48 nm. The catalytic performance of the chromium phosphates was examined by employing a model reaction, namely the dehydration of isopropanol to propene. The results indicated that all synthesized chromium phosphates exhibited significantly higher isopropanol conversions and propene yields than that synthesized via the conventional precipitation route. The highest propene selectivity (96.43%) at the highest isopropanol conversion (93.10%) has been obtained over the mesoporous chromium phosphate catalyst synthesized with a P/Cr atomic ratio of 2.0. The formation

mechanism of the mesoporous chromium phosphate was investigated by FTIR technique. The results show that CTAB template plays a key role in the formation of mesoporous chromium phosphates.

Mesoporous lithium manganese phosphates were also successfully synthesized using the same approach of solid state reaction (SSR) at low temperature by using $LiC_2O_3 \cdot 6H_2O$, $MnCl_2 \cdot 6H_2O$ and $NH_4H_2PO_4 \cdot 2H_2O$ as precursors and the surfactant cetyltrimethyl ammonium bromide (CTAB) as template. The synthesized lithium manganese phosphates were characterized by XRD, EDS, SEM, HR-TEM, N_2-physisorption. The results show that the synthesized meoporous lithium manganese phosphates exhibited a high specific surface area (256.63 m^2/g) and a narrow pore size distribution. The electrochemical tests of Li-ion batteries were performed and the results show that the charge voltage could increase to be 3.60 V while the first time discharge capacity could be as high as 100 mAh/g.

The Nitro-Cu-MOF complexes, a new class of metal organic frameworks, have been successfully synthesized using a conventional thermal reaction. The obtained Nitro-Cu-MOFs have a specific surface area of 576.27 m^2/g and a pore volume of 0.32 m^3/g. The gas uptake of the obtained Nitro-Cu-MOFs at 60 psi is 68 mg/g (sorbate/sorbent) at 298 K for carbon dioxide, which is much higher than that of the Cu-MOFs, 31 mg/g at 298 K for carbon dioxide.

Key Words: Mesoporous phosphates, Synthesis, Solid State Reaction, Lithium manganese phosphates, CO_2 adsorption

1. INTRODUCTION

1.1 Motivation

Phosphate compounds have wide applications in the selective adsorption of metal ions, the catalysis of some organic reactions and li-ion batteries. In recent years, the application of phosphates compounds has a significance increase. The structure and composition of these compounds depends on the synthesis route, which in turn, determines the catalytic and adsorptive performances of these compounds. As a result, various synthesis methods have been studied by practitioners and researchers.

Currently, most phosphates, such as amorphous $CrPO_4$ and crystalline $CrPO_4 \cdot 6H_2O$, were synthesized via the wet chemistry route. Yet, a high surface area is difficult to obtain for both amorphous and crystalline compounds due to agglomeration. Solid state reaction and high-temperature calcination routes for some phosphates have been explored, which usually results in the formation of crystalline phosphates such as $LiFePO_4$ and $LiMnPO_4$. These crystalline phosphates generally have low specific surface areas and low pore volumes.

Mesoporous inorganic materials have some unique properties such as high specific surface area, large pore volume, tunable nanopore sizes, adjustable framework composition, and controllable particle morphology. Phosphates need to be made into mesoporous materials for their application in catalysis and selective adsorption. Since applications in the catalysis industry and li-ion batteries desire a high surface area of phosphates compounds, it is necessary to investigate a typically novel method to synthesize mesoporous phosphates.

Coal-fired power plants currently generate approximately 50% of the electricity in the United States. While coal is a cheap and abundant resource, the continued reliance upon coal as an energy source could potentially have serious consequences in terms of global warming. Capturing carbon dioxide from coal-fired power plants, thereby preventing release into the atmosphere is of fundamental importance. Metal-Organic Frameworks are crystalline compounds consisting of metal ions or clusters coordinated to often rigid organic molecules to form one-, two-, or three-dimensional structures that can be porous. To date, several MOFs have been shown to exhibit exceptional CO_2 storage capacity under equilibrium conditions where pure CO_2 or gas mixture is introduced into the pores. In this thesis, part of research will be focused on the synthesis of Nitro-Cu-MOF complexes, a new class of metal organic frameworks that might show a great potential on the CO_2 storage.

1.2 Objectives

The objective of the current work mainly includes the synthesis and application of the various mesoporous phosphates via a typically novel method. And obtained mesoporous phosphates have been characterized and studied. The detailed objectives could be shown in the following:

- To develop a novel method, solid-state reactions at low temperatures (SSRLT), to synthesize the mesoporous chromium phosphates. The synthesis conditions will be optimized; furthermore, the catalytic performance of chromium phosphates prepared by SSRLT, in terms of activity and selectivity, will be studied.

- To develop the solid-state reactions at low temperatures (SSRLT) to synthesize the mesoporous lithium manganese phosphates. The synthesis conditions will be optimized; furthermore, the electric performance of lithium manganese phosphates prepared by SSRLT will be studied.

- To develop the FTIR technique to study the mechanism of the formation mesoporous phosphates via solid-state reaction at low temperature (SSRLT).

The objective of the current work also includes the synthesis and application of Nitro-Cu-MOFs, a new class of metal inorganic frameworks. The detailed objective could be shown in the following:

- To synthesize the Nitro-Cu-MOFs, a new class of metal organic frameworks, via hydrothermal method, and structure will be characterized by Synchrotron X-ray radiation at ChemMatCARS beamlines. The CO_2 uptake captivity, in terms of weight ratio, will be studied.

1.3 Systems of Interest and Approach

To achieve these objectives, mesoporous chromium phosphates and lithium manganese phosphates will be synthesized via solid state reaction at low temperature by varying different synthesized conditions. The obtained mesoporous phosphates will be initially characterized and studied. Characterization tools include X-ray diffraction, high resolution transmission electron microscopy, nitrogen adsorption-desorption, Ultraviolet-visible diffuse reflection (UV-Vis) spectroscopy, Thermo-gravimetry analysis (TGA) and differential scanning calorimetry(DSC), Fourier transform infrared (FT-IR) spectroscopy.

Chromium phosphates are the typical inorganic materials that could be synthesized via different methods. We selected the sol-gel route to synthesize the mesoporous chromium phosphates for comparison. To evaluate the catalytic performance of the synthesized chromium phosphate compounds, the dehydration of isopropanol to propene was used as a model reaction. The catalytic performance of chromium phosphates prepared by SSRLT, in terms of activity and selectivity, will be compared with those prepared via sol-gel route.

As for the mesoporous lithium manganese phosphates, they will be synthesized via solid state reaction at low temperature by varying different synthesis conditions. The electrochemical test will be performed using home designed cell with lithium foil as the counter electrode, and 1.2M $LiPF_6$ in EC/EMC (3:7 by weight) as the electrolyte, the separator is Celgard 3501 from Celgard Company. The electrochemical property is tested on Solartron SL1260. And the charge/discharge rate of the $LiMnPO_4$ half cell is 0.1 C between 2.8 V to 3.8 V.

For the synthesis of Nitro-Cu-MOF complexes, the CO_2 absorption on the MOF complexes surface will be examined in a home-made system. Briefly, certain amount of activated MOFs (solvent molecules removed under vacuum) will be placed in a stainless steel vessel. The vessel is sealed and weighed using an analytical balance. Ultra-pure carbon dioxide is then introduced into the vessel under various pressures to saturate the MOF complexes. The vessel is then sealed and weighed again. The weight increase observed will correspond to the amount of carbon dioxide absorbed at the surface of the MOF complexes. As well, the CO_2 absorption on the Cu-MOF complexes surface will be also examined for comparison.

2. BACKGROUND

2.1 Mesoporous Materials

2.1.1 Definition of Mesoporous Materials

Porous materials are classified into several kinds by their size. According to IPUAC notation, three different porous materials have been classified: microporous materials have pore diameters of less than 2 nm and macroporous materials have pore diameters of greater than 50 nm; while the mesoporous material is a material containing pore with diameters between 2 and 50 nm. Since the 1940s, naturally porous materials have shown high performance as catalysts, when scientists began to prepare the synthesized porous materials, in which the pore size is limited in 2 nm. Zeolites are the typical example, which include the aluminosilicate members of the family of microporous materials known as “molecular sieves”. Zeolites are widely used as catalysts in the industry [1]. Zeolites confine molecules in small spaces, which cause changes in their structure and reactivity. The hydrogen form of zeolites (prepared by ion-exchange) is powerful solid-state acids, and can facilitate a host of acid-catalyzed reactions, such as isomerisation, alkylation, and cracking [2]. However, the pore size of the zeolites is all limited to 2 nm and does not allow the bigger molecules to pass, which limits their application as catalysts. Porous silica and porous glasses are typically unordered mesoporous materials. Compared to zeolites, the pore size of porous silica and porous glasses is larger, however, their pore structure is anomalous and the pore distribution is very broad, which limits their application in separation, adsorption and catalysis applications. In 1990, Japanese researchers first reported mesoporous materials with a long range order. In 1992, M41S, a series of mesoporous materials, were first synthesized

by Mobil's researchers [3]. Among them, MCM-41 and MCM-48 were studied most. Although they are composed of an amorphours silica wall, they possess a long range ordered framework with uniform mesopores. The surface area could be more than 1000 m^2/g. Moreover, the pore diameter of these materials can be freely controlled within a mesoporous range of 1.5 to 20 nm by adjusting the synthesis conditions and/or by employing surfactants with different chain lengths in their preparation. Zeolites are limited to pore sizes of ~20 Å, while mesoporous materials have material characteristics similar to zeolites, but with larger pores. This combination of material characteristics would be very useful for applications such as adsorption, separation and use in the catalysis industry.

2.1.2 Classification and Characteristics of Mesoporous Materials

According to the different composition, mesoporous materials could be divided into silica mesoporous materials that include some kinds of silica and alumina which have similarly-sized fine mesopores and non silica mesoporous materials including mesoporous oxides, phosphates *et al*. The non silica mesoporous materials, show promise to be used as catalysts due the existence of a Transition-state. However, this kind of mesoporous materials is not stable. The mesopores could collapse after calcination and also the mechanism of synthesis still remains unknown. This causes most scientists to focus their research on silica mesoporous materials.

A mesoporous material can be disordered or ordered in a mesostructure. Just as mentioned above, porous silica and porous glasses are typically unordered mesoporous materials. Their pore structure is unordered and the pore distribution is very wide. While M41S is highly ordered and gives a diffraction pattern but the silicate walls are not crystalline, they are glass-like. The pore size distribution in MCM-41 is usually as narrow as well ordered materials can be made. As a novel ordered nanomaterial, research in this field has steadily grown. Notable examples of prospective applications are catalysis, sorption, gas sensing, optics, and photovoltaics. These applications also include magnetic

fluorescent delivery vehicles, mercury ion detection, drug-delivery systems, bone-tissue engineering, and other potential applications in the medical and environmental fields. The characteristics of ordered mesoporous materials are just between the amorphous disordered materials (such as amorphous silica) and zeolite, with a crystalline structure and uniform pore distribution. Typically, zeolites are limited to pore sizes of 1.5 nm, while for mesoporous materials, the materials characteristics are similar to zeolites but with larger pores, which would be very useful. Normally, the main characteristics of mesoporous materials could be shown in the following:

1) The pore structure is high ordered;

2) The pore size distribution is usually quite narrow. And the pore size can be controlled varying from 1.5 nm~30 nm by changing the composition of the synthesis mixture or surfactants;

3) Huge surface areas, providing a vast number of sites where sorption processes can occur;

4) By using different surfactants, different structure can be formed such as micelles, rods, sheets and 3D structures;

5) After modification, high thermal stability and hydrothermal stability could be obtained.

Here, for example, the pore size distribution in MCM-41 is usually quite narrow as well ordered materials can be made, but it is not as tightly defined as that for a zeolite as MCM-41 is not a crystalline product. And the main characteristics of the MCM-41 are: pore size is about 3.5 nm; pore wall is about 1 nm; the surface area could be as high as 1000 m^2/g and the pore volume is about1 ml/g. Up to now, a lot of work has been done exploring the formation of silicate structures using self assembled templates. And many different mesoporous materials have been synthesized. Mesoporous materials are

classified into several classes by their pore size and structure. A typical example can be seen in Table 2.1.

Table 2.1 Mesoporous materials with different pore structures

Characteristics of pore structure	Structure	Typical example
Lowly ordered, 1D	（hexagonal）	MSU-n, HMS, KIT-1
1D (no pore distribution)		MCM-50
2D lamellar	Hexagonal	MCM-41, SBA-3, FSM-16, TMS-1
3D (cages)	cubic	SBA-1, 6, 16, FDU-2, 12, SBA-11
3D (Intersecting channels)	cubic-hexagonal	SBA-2, 7, 12, FDU-1
	cubic	SBA-16, MCM-48, FDU-5, HUM-7

2.1.3 Synthesis Methods of Mesoporous Materials

So far, a lot of work has been done to synthesize different mesoporous materials. From the initial M41S mesoporous materials to FSM, HMS, MSU, SBA, KIT *et al*., there have been literally thousands of publications dealing with mesoporous ceramics, with a wide variety of synthetic methods being developed. However, depending on the synthesis conditions, the silica source or the type of surfactants that has been used, many mesoporous materials can be synthesized following the co-operative assembly pathway. And there are several synthesis methods which are widely adopted by scientists. Among them, the sol-gel method and hydrothermal method have been adopted most.

2.1.3.1 Sol-gel Method

The sol-gel process, also known as chemical solution deposition, is a wet-chemical technique widely used in the fields of materials science and ceramic engineering. Such methods are used primarily for the fabrication of materials (typically a metal oxide) starting from a chemical solution which acts as the precursor for an integrated network (or gel) of either discrete particles or network polymers. The sol-gel method has also been widely used in the synthesis of mesoporous materials, during the synthesis, different template could be used as the template such as cation surfactants, triblock copolymers and organic small molecules. Ryoo *et al.* reported that by using CTAB (a kind of cation surfactants) as the template and sol-gel method, the mesoporous silica molecular sieve MCM-41 can be obtained in a highly ordered form with various pore diameters of micelle packing is suitably controlled with a mixture of n-alkyltrimethylammonium bromide and nalkyltriethylammonium bromide according to the length of the C_{12}–C_{22} alkyl groups [4]. Zhao *et al.* reported that by the use of amphiphilic triblock copolymers to direct the organization of polymerizing silica species has resulted in the preparation of well-ordered hexagontal mesoporous silica structures (SBA-15) with uniform pore sizes up to approximately 300 angstroms, and also the morphology and pore size distribution could be controlled [5]. Wei *et al.* reported that by using organic small molecule like glucose as the template, well-ordered mesoporous materials could be obtained [6].

2.1.3.2 Hydrothermal Methods

Hydrothermal synthesis can be defined as a method of synthesis of single crystals which depends on the solubility of minerals in hot water under high pressure. The crystal growth is performed in an apparatus consisting of a steel pressure vessel called autoclave, in which a nutrient is supplied along with water. A gradient of temperature is maintained at the opposite ends of the growth chamber so that the hotter end dissolves the nutrient and the cooler end causes seeds to take additional growth. Hydrothermal method has also been widely used in the synthesis of mesoporous materials. Mizuno *et al.* has obtained the mesoporous V-P-O mesoporous materials by using the hydrothermal method, and

also the morphology of obtained materials could be controlled via changing the pH value [7].

Meanwhile, other methods have also been adopted in the synthesis of mesoporous materials. Yao *et al.* reported that by using the CTAB as the template, MCM-41 mesoporous materials could be obtained via microwave heating [8]. And the results show that that by microwave heating, high ordered mesoporous materials could be obtained via in a very short time. The microwaves provide intense localized heating that may be higher than the recorded temperature of the reaction vessel. At some time, microwave is a promising way for synthesizing mesoporous materials as well as other nanomaterials.

2.2 Solid State Reaction

2.2.1 Introduction to the Solid State Reaction

In the beginning of 20^{th} century, solid state chemistry has been recognized as a separate science. The solid state chemistry is the study of the synthesis, structure, and physical properties of solid materials. It therefore has a strong overlap with solid-state physics, mineralogy, crystallography, ceramics, metallurgy, thermodynamics, materials science and electronics with a focus on the synthesis of novel materials and their characterization. A solid state reaction, also called a dry media reaction or a solventless reaction, is a chemical reaction in which solvents are not used. In a normal reaction, the reacting agents, also called the reactants, are placed in a solvent before the reaction can take place. These reactants react to form a new substance. After the reaction is completed, scientists are able to remove the new product from the solvent. Basically, the normal reaction is time and energy consumption, and also not environmental friendly. A solid-state reaction, however, allows the reactants to chemically react without the presence of a solvent. It is important to economics because the elimination of solvents means that products will cost less. With normal reactions, scientists need to remove the residual

solvent from the resulting product after a reaction has finished. Producing materials from a solid state reaction will mean that scientists are able to bypass the purification process. So scientists began to focus on the solid state reaction method especially on the solid state reaction method at low temperature. Up to now, solid state reaction method has already been one of the most important methods for synthesis of nanomaterials.

2.2.2 Classification of Solid State Reaction Method

Solid state reaction methods are classified into several kinds by their different reaction temperature.

2.2.2.1 High Temperature Solid State Reaction

For high temperature solid state reaction, the reaction temperature is above 300 ℃. Although scientist cannot obtain ideal materials completely, the high temperature solid state reaction still holds a dominant position in the materials synthesis. For example, bulk solids are prepared using tube furnaces, which allow reactions to be conducted up to ca. 1100 ℃. Special equipment e.g. ovens consisting of a tantalum tube through which an electric current is passed can be used for even higher temperatures up to 2000 °C. Such high temperatures are at times required to induce diffusion of the reactants, but this depends strongly on the system studied. Another good example of a high temperature solid state reaction is the “melt method”. One method often employed is to melt the reactants together and then later anneal the solidified melt.

2.2.2.2 Low Temperature Solid State Reaction

For low temperature solid state reaction, the reaction temperature is below 300 ℃. Since the reaction temperature is much lower, scientists begin to focus their research on the material’s synthesis at low temperature. Hou once reported ZnO nanorods synthesis by solid state reaction. These ZnO nanorods were prepared between anhydrous zinc

sulfate and sodium hydroxide in the absence of surfactant and template at relatively low temperature. And the results showed that when Zn^{2+}/OH^{-} ratio was 1:4, good rod-like morphology with the diameter of 30 – 50 nm and length of ca. 600 nm can be obtained [9]. Li once reported that nanosized MnO could also be prepared via solid state reaction route at room temperature. The MnO particles were acicular, in the size range 50 nm, and with large specific area which is as high as1200 m^2/g [10]. Normally, solid state reaction is very promising in the materials synthesis. And there is no report about the synthesis of mesoporous materials via solid state reaction at low temperature.

2.3 Phosphates

2.3.1 Introduction to Phosphates

A phosphate, an inorganic chemical, is a salt of phosphoric acid. In organic chemistry, a phosphate, or organophosphate, is an ester of phosphoric acid. Organic phosphates are important in biochemistry and biogeochemistry or ecology. Inorganic phosphates are mined to obtain phosphorus for use in agriculture and industry. At elevated temperatures in the solid state, phosphates can condense to form pyrophosphates. Phosphates are utilized for detergents, food additives, fertilizers, corrosion inhibitors, etc. as bulk materials, and for adsorbents, catalysts, chemical sensors, etc .as surface-functional materials. The interaction of some guest molecules with the surface of a host functional phosphate results in (1) adsorption on the surface, (2) activation of the adsorbed molecules, (3) chemical reaction on the surface, (4) change in electric or electronic properties of the host phosphate, etc.

2.3.2 Application of Phosphates as a Cathode in the Li-ion Batteries

The lithium-ion battery is a kind of rechargeable battery, in which lithium ions move from the negative electrode to the positive electrode during discharge, and back

when charging. Lithium-ion batteries are common in consumer electronics. They are one of the most popular for portable electronics, with one of the best energy-to-weight ratios, no memory effect, and a slow loss of charge when not in use. Beyond consumer electronics, LIBs are growing in popularity for national defense, electric vehicles, and aerospace applications due to their high energy density. Research is yielding a stream of improvements to traditional LIBs technology, focusing on energy density, durability, cost, and safety.

Recently, Lithium transition-metal (ortho) phosphates have attracted attention as potential Li-ion battery cathode materials due to their lower toxicity, lower cost and better chemical and thermal stability, when compared to the currently used $LiCoO_2$. In 1996, Goodenough and coworkers identified lithium iron phosphate ($LiFePO_4$) and other phospho-olivines (lithium metal phosphates with olivine structure) as cathode materials [11]. Because of its low cost, non-toxicity, the high abundance of iron, its excellent thermal stability, safety characteristics, good electrochemical performance, and high specific capacity (170 mA·h/g, or 610 C/g) it gained some market acceptance. Chiang and his group at MIT reported that a dramatic improvement in the performance of lithium batteries has been obtained by boosting the material's conductivity by doping it with aluminum, niobium and zirconium [12]. The exact mechanism causing the increase became the subject of a heated debate. In 2004, Chiang again reported that an increased performance by utilizing iron-phosphate particles of less than 100 nanometers in diameter [13]. This decreased particle density by almost one hundredfold, increased the cathode's surface area and improved capacity and performance. Indeed $LiFePO_4$ has been extensively investigated, and is now present in commercial cells for high power, and large format applications.

Encouraged by the success of $LiFePO_4$, $LiMnPO_4$ is also attracting increased attention. Lithium manganese phosphate has a redox potential of 4.1 V versus Li^+/Li, which is considered to be the maximum limit accessible to most liquid electrolytes. This is ~0.65 higher than $LiFePO_4$, The high ionic and electronic resistance of $LiMnPO_4$ have rendered it difficult to obtain high electrochemically activity. Li *et al*. first reported the

reversible reaction of Mn(II)↔Mn(III) in olivine phosphate. Their material presented a reversible capacity of ~140 mA·h g^{-1} at C/15 within 2.0–4.5 V vs. Li/Li^+. Although several groups have explored various methods to prepare electro-active $LiMnPO_4$, there are very few reports of performance greater than 100 $mAh \cdot g^{-1}$ [14 - 15].

2.3.3 Synthesis Methods for Metal Phosphates

2.3.3.1 Hydrothermal Chemistry Method

Hydrothermal (HDT) chemistry is one of the principal synthetic methods for the preparation of metal phosphates. It is used to produce various metal phosphates such as chromium phosphates, lithium ion phosphates and lithium magnesium phosphates which are functional in catalysis, electrochemistry and separation science. These compounds may have intriguing morphologies such as nanospheres, nanowires and nanotubes. Control of the products comes as a result of careful manipulation of concentration, pH and temperature.

2.3.3.2 Solid State Reaction at High Temperature

Solid state reaction route at high-temperature for metal phosphates synthesis has been explored for decades. For the synthesis of chromium phosphates, the formation of crystalline α-$CrPO_4$, β-$CrPO_4$, $Cr(PO_3)_3$, $Cr_3(PO_4)$, $Cr_2P_2O_7$, $Cr_7(PO_4)_6$, $Cr_6(P_2O_7)_4$, and $Na_{17}Cr_9P_{12}O_{58}H_{12}$ is normally obtained by using the solid state reaction at high temperature [16 - 19]. For the synthesis for $LiMnPO_4$ and $LiFePO_4$, the formation of olivine structure $LiMnPO_4$ and $LiFePO_4$ is normally obtained via solid state reaction at high temperature [15, 20 - 24]. Although scientist cannot obtain ideal materials completely, the high temperature solid state reaction still held a dominant position in the materials synthesis via solid state reaction.

These crystalline metal phosphates generally have low specific surface areas and low pore volumes. However, the use of solid-state reactions to synthesize the mesoporous materials at low temperatures has not been reported yet. Here, we present our work on employing the solid-state reactions at low temperatures (SSRLT) in synthesis of mesoporous chromium phosphates and mesoporous lithium magnesium phosphates.

3. SYNTHESIS OF MESOPOROUS CHROMIUM PHOSPHATES VIA SOLID STATE REACTION AT LOW TEMPERATURE

3.1 Introduction

Chromium phosphate compounds, with the introduction of metal ion via ion exchange, show a promising activity in organic reactions, such as: 1) the dehydration of alcohols, 2) the oxidative dehydrogenation of alkanes, 3) the isomerization of alkenes, and 4) the alkylation of aromatics. The synthesis route, among other factors, plays an important role in the structure formation as well as the textile properties, like BET surface area, pore volume, and pore size distribution, which are vital to adsorption and activation of reactants. Currently, most chromium phosphates, such as amorphous $CrPO_4$ and crystalline $CrPO_4 \cdot 6H_2O$, $Cr(H_2O)_4HP_2O_7 \cdot 3H_2O$, and $Na_2CrP_2O_7 \cdot 0.5H_2O$ [25], are commonly synthesized via the wet chemistry route, while a high surface area is difficult to be obtained either amorphous or crystalline compounds because of agglomeration during preparation.

Mesoporous inorganic materials have some valuable properties such as high specific surface area and pore volume, with controllability in nano-pore sizes, framework composition, and particle morphology. Mesoporous chromium phosphates can be synthesized via the sol-gel method. This technique facilitates the controllable hydrolysis and condensation of precursor species, via the supramolecular assembly of surfactant micelles, generating mesoporous materials with a homogeneous distribution of components at molecular level. Using the sol-gel technique, various mesoporous silicas such as M41S, SAB-n, MSU-X, and HMS, and numerous non-silica mesoporous materials of single metal oxides, mixed metal oxides, and aluminophosphates have been

synthesized. Very recently, Tarafdar *et al*. reported the synthesis of mesoporous chromium phosphate via the sol-gel route [26].

Just as mentioned above, the textile properties of chromium phosphate could be determined via the synthesis route. Solid state reaction and high-temperature calcination routes for chromium phosphates have been explored, which usually results in the formation of crystalline α-$CrPO_4$, β-$CrPO_4$, $Cr(PO_3)_3$, $Cr_3(PO_4)$, $Cr_2P_2O_7$, $Cr_7(PO_4)_6$, $Cr_6(P_2O_7)_4$, and $Na_{17}Cr_9P_{12}O_{58}H_{12}$ [16 - 19]. These crystalline chromium phosphates generally have low specific surface areas and low pore volumes. Though synthesis of mesoporous chromium phosphates, which have high specific surface areas and pore volumes, could be obtained via the sol-gel route, the sol-gel techniques offers some disadvantages over solid state reaction technique, for instance, more steps, complex operating conditions, and non-environmental friendly. So to explore a new route for synthesizing mesoporous chromium phosphates is desired. Currently, the use of solid-state reactions to synthesize the mesoporous materials at low temperatures has not been reported yet. Here, we present our work on employing the solid-state reactions at low temperature (SSRLT) in synthesis of mesoporous chromium phosphates. The synthesized mesoporous chromium phosphates have better textural properties, compared with those prepared via the conventional sol-gel route. Meanwhile, the catalytic performance of chromium phosphates prepared by SSRLT, in terms of activity and selectivity, is significantly better than that of those prepared via sol-gel routes.

3.2 Overview

The general structure of this chapter includes the preparation of chromium phosphates via solid state reaction at low temperature and their structure and catalytic characterization. Characterization tools include X-ray diffraction, high resolution transmission electron microscopy, nitrogen adsorption-desorption, Ultraviolet-visible diffuse reflection (UV-Vis) spectroscopy, Thermo-gravimetry analysis (TGA) and differential scanning calorimetry (DSC). To evaluate the catalytic performance of the

synthesized chromium phosphate compounds, the dehydration of isopropanol to propene was used as a model reaction. The identification of the products was achieved using a Varian Saturn-2200 GC-MS equipped with a DB-1 capillary column (30 m × 0.25 mm × 0.25 μm). The quantitative analysis of the products was performed using a Perkin Elmer Clarus 500 GC equipped with a thermal conductivity detector (TCD) and a HayeSep DB column (30′ × 1/8″ × 0.085″).

3.2.1 X-ray Diffraction

The structure of the synthesized compounds was determined using X-ray diffraction (XRD) (Brucker D8 advance diffractometer, Cu Kα radiation, wavelength 1.5406 Å). The diffraction data were recorded for 2θ angles between 0.35 and 75°, with a scanning speed of 0.02° /sec.

3.2.2 High Resolution Transmission Electron Microscopy

The morphology of the synthesized compounds was examined using high resolution transmission electron microscopy (HR-TEM) (JOEM-3010 electron microscope). Energy dispersible X-Ray spectroscopy (EDS) with an elemental analysis accessory (OXFORD) was used to analyze the local composition of the synthesized compounds.

3.2.3 Nitrogen Adsorption-desorption

The BET surface area and porosimetry of the synthesized compounds were measured using nitrogen adsorption-desorption (Beckman Counter SA 3100). Before adsorption measurements, the specimen was heated from room temperature up to 573 K, evacuated to 10^{-3} Pa, and then kept at that temperature and under that vacuum outgasing for 2 h. The specific surface area was determined by the BET method, and the pore size

distribution was obtained from the N_2-desorption curve by the BJH (Barrett-Joyner-Halenda) method.

3.2.4 Ultraviolet-visible Diffuse Reflection Spectroscopy

The oxidation state of chromium in the chromium phosphates was determined using Ultraviolet-visible diffuse reflection (UV-Vis) spectroscopy (Perkin Elmer Lambda 35 UV-Vis spectrometer). Data has been collected between 200 - 800 nm using $BaSO_4$ as a reference. The thermal stability of the synthesized compounds was characterized using Thermo-gravimetry analysis (TGA) and differential scanning calorimetry (DSC) (Netzsch STA449C). The specimen was heated from room temperature to 1273 K at a rate of 5 ^oC/min, with a 98.5% N_2 carrier gas at a flux of 50 ml/min.

3.2.5 Catalytic Performance Evaluation

To evaluate the catalytic performance of the synthesized chromium phosphate compounds, the dehydration of isopropanol to propene was used as a model reaction. Before testing, the chromium phosphate specimen was calcined at 823 K to remove the CTAB. The reaction was performed in a fixed-bed flow-type quartz reactor under the following conditions: catalyst amount = 1.0 g; flow rate of isopropanol ($\geq$ 99.7%) = 0.085 ml/min; reaction temperature = 473 ~ 563 K (at 30 K intervals); atmospheric pressure. The effluent from the reactor was cooled in an ice bath in which the gaseous products and residual isopropanol were separated. After the reaction proceeded smoothly for 60 min, both the liquid and the gases in the ice bath were sampled and analyzed. The identification of the products was achieved using a Varian Saturn-2200 GC-MS equipped with a DB-1 capillary column (30 m × 0.25 mm × 0.25 μm). The quantitative analysis of the products was performed using a Perkin Elmer Clarus 500 GC equipped with a thermal conductivity detector (TCD) and a HayeSep DB column (30′ × 1/8″ × 0.085″). The conversion of isopropanol and the selectivities to the reaction products were calculated as shown in the Appendix.

3.3 Experiment

3.3.1 Objectives

A set of chromium phosphates were synthesized via conventional sol-gel route according to the procedure reported in literatures to set as standard chromium samples. Several samples with different P/Cr ratio were synthesized with solid state reaction at low temperature. The set of samples were accordingly synthesized and characterized with the tools described as to the aforementioned methods and settings.

3.3.2 Synthesis of $CrPO_4$ via Conventional Sol-gel Route

A solution containing chromium and phosphate was first prepared by dissolving equal moles of $CrCl_3 \cdot 6H_2O$ (Analytical reagent, A.R., Sigma Aldrich) and $NaH_2PO_4 \cdot 2H_2O$ (Analytical reagent, A.R., Sigma Aldrich) into distilled water at 273 K, and then a cold ammonium aqueous solution (25 % volume) was added with continuous stirring. The resulting precipitate was aged at room temperature for 24 h, then recovered by filtration, washed thoroughly with distilled water, and dried at 373 K for 24 h. Finally, the synthesized chromium phosphates were calcined at 823 K for 6 h.

3.3.3 Synthesis of Mesoporous $CrPO_4$ via SSRLT Route

$CrCl_3 \cdot 6H_2O$ (Analytical reagent, A.R., Sigma Aldrich) and $NaH_2PO_4 \cdot 2H_2O$ (Analytical reagent, A.R., Sigma Aldrich) in various P/Cr molar ratios were mixed together and grinded in a mortar for 20 minutes, and then mixed further with a selected amount of cetyltrimethyl ammonium bromide (CTAB) and grinded together for another 15 minutes. The obtained mixtures with atomic ratios of P: Cr: CTAB = x: 1.0: 0.001, where x = 1.0, 1.6, 1.8, 2.0, 2.2, 2.4 and 3, were transferred into beakers for heating at 373 K for 24 h. After cooling to room temperature, the samples were washed thoroughly

with distilled water and then dried at 373 K for 24 h. To remove the surfactant, the specimens were further calcined in N_2 at 823 K for 6 h.

3.4 Results and Discussion

3.4.1 X-ray Diffraction

The XRD pattern of the chromium phosphate synthesized via the conventional sol-gel route (data not shown here) reveals that the chromium phosphate was amorphous phase. This result is consistent with what Bautista *et al.* Found [27]. As shown in Figure 3.1, the samples prepared by SSRLT were scanned by XRD. The curves indicated that, among the samples with various P/Cr atomic ratios, containing surfactant CTAB, there is no diffraction peak around $2\theta = 2°$ over chromium phosphates with a P/Cr atomic ratio < 1.8 (Figure 3.1 a and b), which suggesting the absence of a mesophase. A single diffraction peak starts around $2\theta = 2°$, over the sample with a P/Cr atomic ratio = 1.8, and intensifies with the increase in the atomic ratio until the atomic ratio = 2.0 (Figure 3.1 c to d). Further increase of the P/Cr resulted in the peak broadening and peak position shifting (Figure 3.1 e to g), indicating the broadening of the mesopore size distribution, possibly due to the enlargement of the mesopores and/or the thickening of the walls of the pores. The synthesized chromium phosphates from an initial batch with an atomic ratio of P/Cr = 2.0 possessed the maximum ordering of the mesopore array (as shown in Figure 3.1 TEM image). Wide angle XRD was also carried out for all the chromium phosphates, but no diffraction peaks were detected (data not shown here), suggesting that all the chromium phosphates have an amorphous structure. The XRD characterization of the chromium phosphate synthesized via SSRLT clearly shows that the pore structure of the synthesized chromium phosphates changes with the P/Cr atomic ratios from a non-mesophase pore to a mesophase pore. The crystal structure of the synthesized chromium phosphates is not a crystalline phase; rather, it is an amorphous phase.

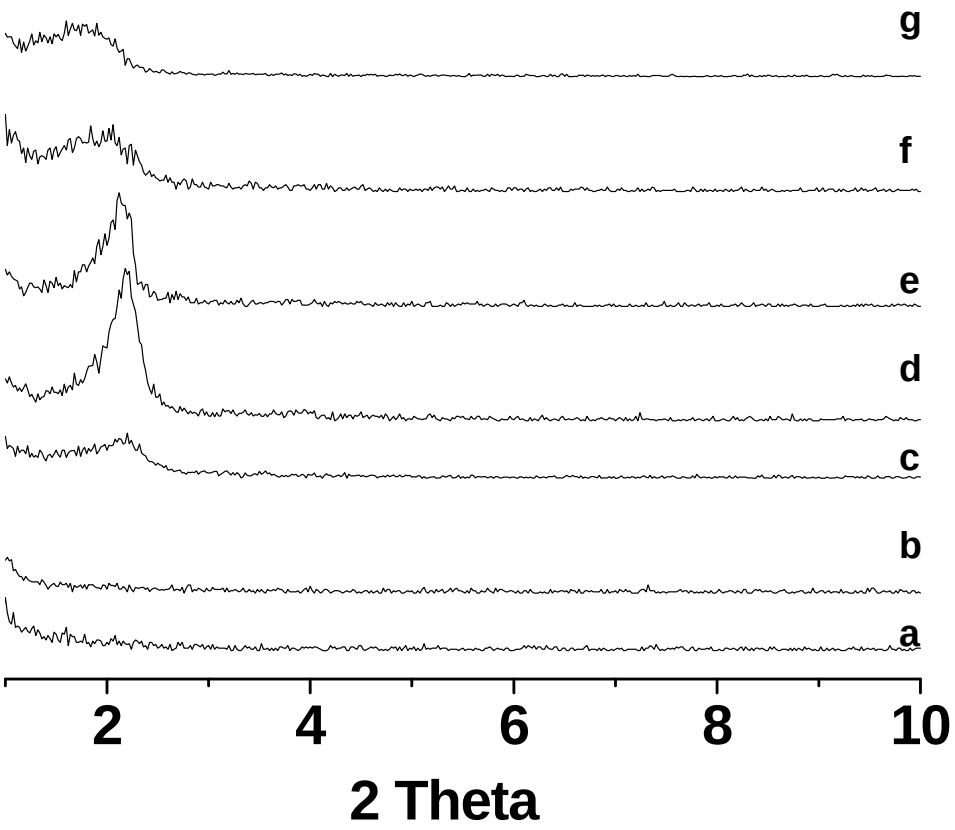

Figure 3.1 XRD patterns of chromium phosphate specimens synthesized before the surfactant removal

The low angle portion of the XRD patterns of the chromium phosphates synthesized via the SSRLT route (with various P/Cr atomic ratios and removed CTAB surfactant) is also shown in Figure 3.2. It is clear that the chromium phosphates synthesized via the SSRLT route have a similar XRD peak pattern (Figure 3.2 a - g), in terms of peak shape and peak position changing with P/Cr atomic ratio, to that of a removed CTAB but with a much stronger peak intensity for the synthesized chromium phosphates containing CTAB. Note that the surfactant CTAB has been removed from these synthesized chromium phosphates through calcination. Thus, the XRD spectrum suggests that the mesostructure is retained after the surfactant CTAB has been removed

and the d-spacing (i.e. average distance between the centers of pores) of the mesophase decreases from ca.4.0 ~ 4.3 to ca. 3.5 ~ 3.86 nm, as compared with those containing the CTAB surfactant. Similarly, no diffraction peaks were detected in the high angle range for these synthesized chromium phosphates.

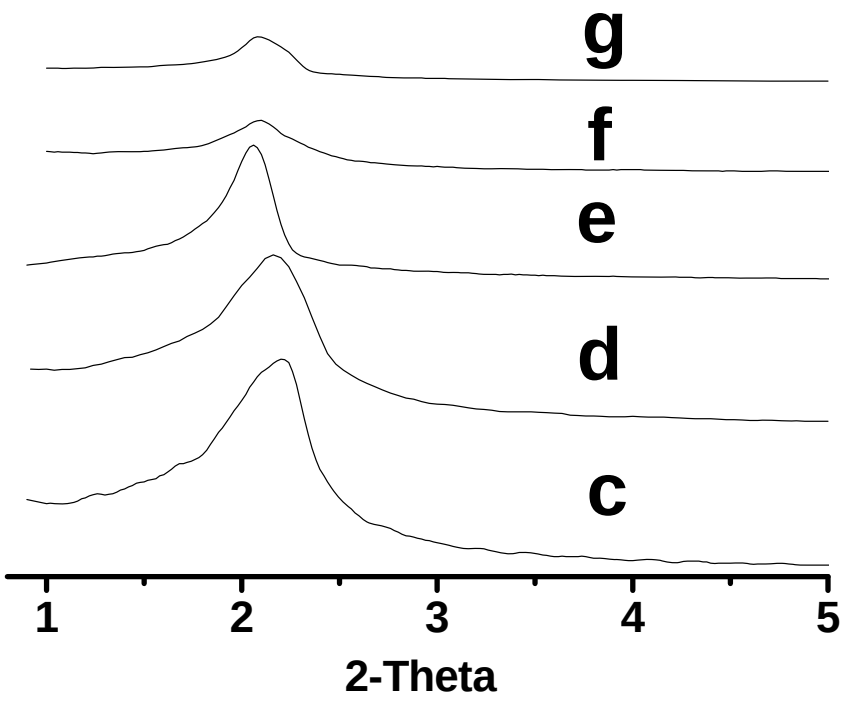

Figure 3.2 XRD patterns of chromium phosphates synthesized after the surfactant removal

3.4.2 HR-TEM and EDS Results

As shown in Figure 3.3, the HR-TEM micrograph of a mesoporous chromium phosphate synthesized via the SSRLT route (with P/Cr atomic ratio = 2 and removal of CTAB surfactant) shows a very orderly arranged wormhole-like pore array structure, which confirms the presence of a mesophase according to the XRD data. One possible mechanism for the formation of such a structure is that the surfactant CTAB and chromium phosphate form a uniform and orderly solid array, which consists of the rod-like micelles of CTAB surrounded by chromium phosphates. Then a uniform and orderly pore array structure is formed when the rod-like micelles of CTAB are removed from this

solid array through calcinations. Thus, the surfactant CTAB plays an important role in the pore structure of chromium phosphates. In addition, the mesopores exhibit mostly wormhole-like pore geometry, with the average distance between the centers of the wormhole-like pores of ca. 3.8 nm, which correlates well with the results from the XRD data.

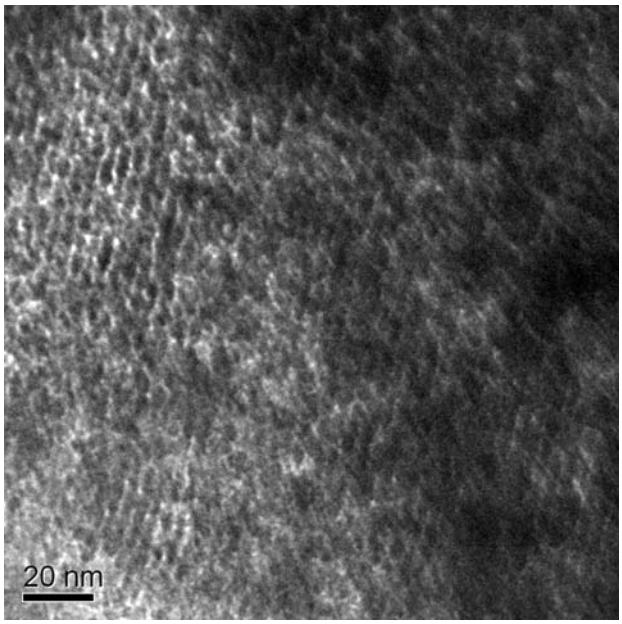

Figure 3.3 HR-TEM micrograph of a mesoporous chromium phosphate prepared with an atomic ratio of P/Cr = 2.0 after the surfactant removal.

Table 3. 1 EDS results and d-Spacings in Å obtained from XRD

	P/Cr in the initial batches						
	1.00	1.60	1.80	2.00	2.20	2.40	3.00
P/Cr in the specimens	1.06	N.D	1.79	2.00	N.D.	2.31	3.03
O/P in the specimens	3.66	N.D.	4.76	4.69	N.D.	4.71	3.89
d-spacing of the specimens	N.A	N.A	4.04	4.13	4.17	4.52	5.17

** N.D.: not determined; N.A.: not available.*

The P/Cr and O/P atomic ratios in the chromium phosphates synthesized via the SSRLT route were determined using EDS. All results are listed in Table 3.1. The results show that the P/Cr atomic ratios in the synthesized specimens are approximately equal to those in the initial batches, and the O/P atomic ratios are around 4. It is clear that the chemical compositions of synthesized chromium phosphates correlate well with the theoretical values.

3.4.3 BET Results

The nitrogen adsorption-desorption isotherm and the pore size distribution curve (in the inset) of the mesoporous chromium phosphate synthesized via the SSRLT route (with P/Cr atomic ratio = 2) is shown in Figure 3.4. The isotherm can be ascribed to type IV in the IUPAC classification and indicates a typical mesostructure. The desorption hysteresis loop corresponds to type H2, and is caused by pore blocking effects during desorption, indicating an ink-bottle pore geometry of the mesostructure. From Figure 3.4, a sharp increase of the volume adsorbed at very low relative pressures (P/P_0) is observed, indicating that the walls of the mesophase pore contain micropores. The BET specific surface area is 250.78 m^2/g and the pore volume is 0.2069 cm^3/g, which have been calculated, based on the adsorption in the relative pressure ranging from 0.05 to 0.2 and the relative pressure of 0.9814, respectively. The mesoporous chromium phosphate has a uniform and narrow pore size distribution, with most of the pore sizes centering around 3.48 nm. The mesoporous chromium phosphate synthesized between 353 and 393 K via the sol-gel route had a specific surface area of 384 m^2/g and a pore volume of 0.2937 m^2/g [26]. However, when this chromium phosphate mesoporous material was heat treated at 823 K for 4 h, the specific surface area decreased rapidly to 201 m^2/g due to the thermal collapse of the mesostructure. In this SSRLT work, the mesoporous chromium phosphate has been calcined at 823 K for 6 h to remove the surfactant before the N_2-physisorption measurements. It is therefore reasonable to conclude that the mesoporous chromium phosphate synthesized via the SSRLT route is thermally more stable and possesses a higher specific surface area than that prepared via the sol-gel route.

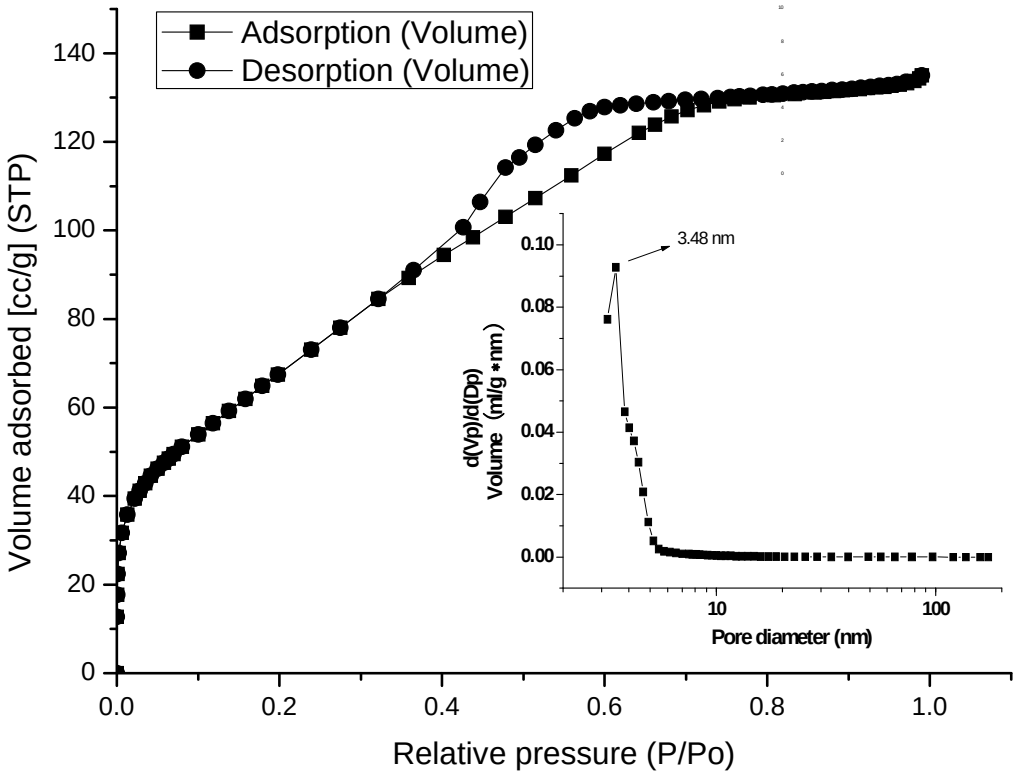

Figure 3.4 Adsorption-desorption isotherm and pore size distribution curve (the inset) of a mesoporous chromium phosphate with an atomic ratio of P/Cr = 2.0

3.4.4 TGA and EDS results

The result of the thermal analysis on the mesoporous chromium phosphate synthesized via the SSRLT route (with P/Cr atomic ratio = 2 and removal of CTAB) is shown in Figure 3.5.

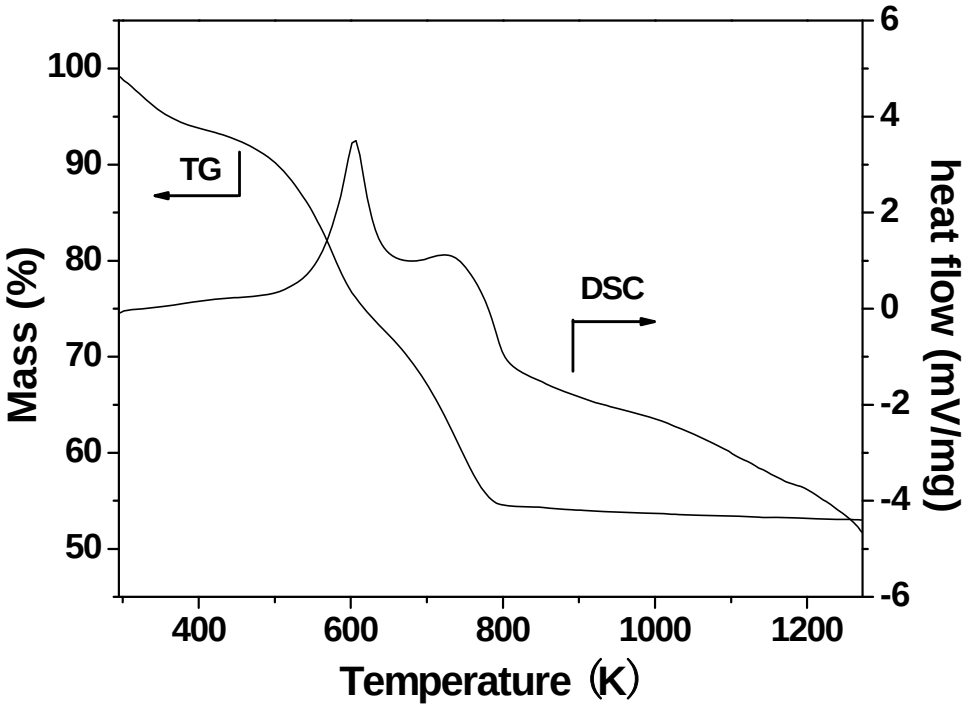

Figure 3.5 TG-DSC curves for the mesoporous chromium phosphate synthesized an atomic ratio of P/Cr = 2.0

The weight loss amounting to 6.5 wt. % in the TG curve below 423 K is due to dehydration, and correspondingly, a small and broad endothermic band is present in the DSC curve in this temperature range. From 423 to 683 K, a weight loss of 24.5 wt. % is observed in the TG curve, and an endothermic peak-centered at 603 K is present in the DSC curve. This peak can be ascribed to the decomposition of the long-chain alkyl group of the surfactant CTA cation. A weight loss of 14 wt. % is observed in the temperature range of 683 to 793 K in the TG curve, and correspondingly, an endothermic peak centered at 733 K in the DSC curve is present. This peak is attributed to the decomposition of the head-group of the surfactant CTA cations. For temperatures higher than 793 K, a weigh loss of as small as 2 wt. % is observed in the TG curve along with a very broad exothermic band in the DSC curve. This may be due to the gradual phase transformation (from ordered mesophase to distorted mesophase) of the mesoporous chromium phosphate for temperatures above 793 K.

3.4.5 UV-Vis Results

Figure 3.6 presents the UV-Vis spectrum of a mesoporous chromium phosphate prepared from an initial batch with a molar ratio of P/Cr = 2.0, after the CTAB removal. Having a d^3 electronic configuration, the Cr(III) ion usually has an octahedral coordination, due to its high crystal field stabilization energy. Theoretically, the UV-Vis spectrum of the Cr(III) ion in the octahedral crystal field exhibits mainly three spin-allowed *d-d* electron transitions $^4A_{2g}(F) \rightarrow {}^4T_{1g}(P)$, $^4A_{2g}(F) \rightarrow {}^4T_{1g}(F)$ and $^4A_{2g}(F) \rightarrow {}^4T_{2g}(F)$ at 290, 450 and 664 nm, respectively, and several spin-forbidden transitions. Ravikumar *et al.* [28] detected the above three spin-allowed transitions at 290, 450, and 664 nm in the UV-Vis spectrum of Cr(III) doped on a zinc phosphate glass substrate. In addition, the 664 nm band exhibits two dips, and a fine structure, at ca. 650 and 687 nm, due to the spin-forbidden transitions $^4A_{2g}(F) \rightarrow {}^2E_{2g}(G)$ and $^4A_{2g}(F) \rightarrow {}^2T_{1g}(G)$. Depending on the substrate and/or coordination environment in which Cr(III) ions are located, red- or blue-shifts can occur for the above bands, and only some of the above bands could be detected in the chromium-containing compounds [29 - 30]. In Figure 3.6, all the above five bands at 290, 445, 665, 640, and 688 nm have been detected, and they can be ascribed to the *d-d* electron transitions from $^4A_{2g}(F)$ to $T_{1g}(P)$, $^4T_{1g}(F)$, $^4T_{2g}(F)$, $^2E_{2g}(G)$, and $^2T_{1g}(G)$, respectively. This suggests that, in the mesoporous chromium phosphate prepared via the SSRLT route, the Cr(III) ions are highly dispersed and have an octahedral coordination. EDS has revealed that the specimen has atomic ratios P/Cr = 2.0 and O/P = 4.69 (see Table 3.1). One can conclude that two phosphates (providing two oxygen coordinates per phosphate) and 1 ~ 2 water molecules (providing one oxygen coordinate per water) generate an octahedral coordination environment around the Cr(III) ion in the mesoporous chromium phosphate. The bands at 420 and 480 nm, as shoulders of the band $^4A_{2g}(F) \rightarrow {}^4T_{1g}(F)$, are probably caused by the different micro-environments around the Cr(III) ions in the mesoporous chromium phosphate. The slight distortion of the octahedral coordination, due to the partial loss of water molecules around some Cr(III) ions, might be a possible cause. In addition, a strong band at 215 nm and a weak band at 335 nm were identified in Figure 3.6. The strong bands at ca. 270 and 340 nm have been usually attributed to an O → Cr(VI) charge transfer and/or to a polychromate species [31

– 35]. Because the band at ca. 270 nm could not be detected and at 335 nm is very weak (Figure 3.6), the content of the Cr(VI) ions and/or the polychromate species in the mesoporous chromium phosphate is expected to be low. It is well known that the oxidized states Cr(IV) and Cr(V) are rather unstable and Cr(V) can easily disproportionate into Cr(III) and Cr(VI). In addition, Cr(II) ions are strong reducing agents and are stable only in the absence of oxygen. Therefore, it is reasonable for us to assign the bands at 210 nm and 335 nm to the O → Cr(III) charge transfer.

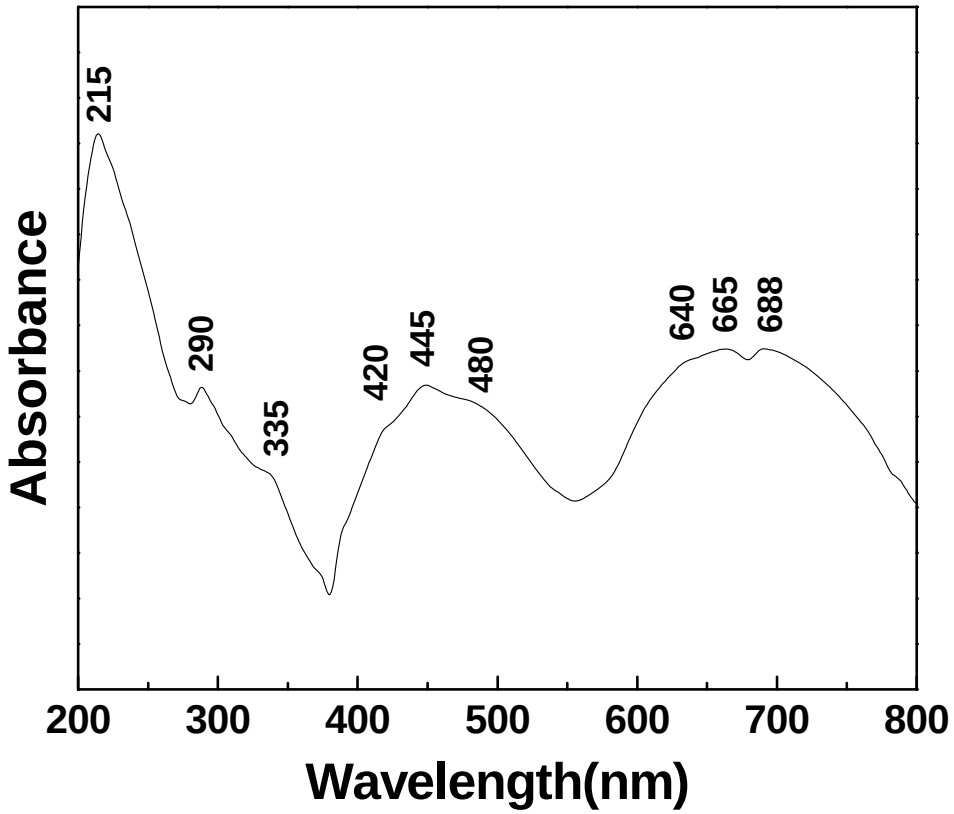

Figure 3.4 UV-Vis spectrum of a mesoporous chromium phosphate prepared with an atomic ratio of P/Cr = 2.0 after the surfactant removal

3.4.6 Catalytic Performance

Table 3.2 shows the effects of reaction temperature on isopropanol dehydration to propene over the mesoporous chromium phosphate catalyst synthesized via the SSRLT

route from an initial batch with an atomic ratio of P/Cr = 2.0. It was found that with an increase in reaction temperature, the isopropanol conversion increases, but the propene selectivity exhibits a maximum at 533 K.

Table 3.2 Effect of reaction temperature on isopropanol dehydration.

Temperature	X	S_i (%)		Y
(K)	(%)	Propene	Diisopropyl ether	(%)
473	33.14	71.34	28.66	23.64
503	58.97	94.66	5.34	55.82
533	93.10	96.43	3.57	89.78
563	96.37	86.33	13.67	83.19

Note: X = conversion of isopropanol; S_i, selectivity to component i; Y is the yield of propene

Table 3.3 presents the results of isopropanol dehydration to propene at 533 K over chromium phosphate catalysts synthesized via the SSRLT and the conventional precipitation pathways. A propene selectivity of 87.70% at an isopropanol conversion of 39.33 % was obtained on the catalyst synthesized via the conventional precipitation route from an initial batch with an atomic ratio of P/Cr = 1.0. This result is superior to that reported in *ref.* [36], where a propene selectivity of ca. 78% at an isopropanol conversion of ca. 6% was attained. Compared to the catalyst synthesized via the conventional precipitation route, the performance of the calcinated catalyst synthesized via the SSRLT route is much better. A propene selectivity of 90.74% at an isopropanol conversion of 50.49% was obtained on the catalyst synthesized from an initial batch with an atomic ratio of P/Cr = 1.0. By increasing the P/Cr ratio, both the isopropanol conversion and the propene selectivity first increase and then are followed by a decrease. The highest propene selectivity (96.43%) and isopropanol conversion (93.10%) was achieved on a catalyst with an atomic ratio of P/Cr = 2.0. XRD revealed that for an atomic ratio of P/Cr $\geq$ 1.8 the catalyst possesses a mesostructure, while the highest crystallinity of the mesophase appeared for an atomic ratio of P/Cr = 2.0. For atomic ratios of P/Cr < 1.8, the

structure was amorphous. Therefore, the mesostructure of chromium phosphate catalysts contributes in an important way to its catalytic performance in the dehydration of isopropanol to propene, mostly due to the high crystallinity, high surface area, high active centers/phase, and accessibility of the active sites of the catalyst.

Table 3.3 Dehydration of isopropanol to propene over different $CrPO_4$.

Catalysts		X	S (%)		Y
Synthesis route	P/Cr molar ratio in initial batch	(%)	Propene	Diisopropyl ether	(%)
SSRLT	1	50.49	90.74	9.26	45.82
SSRLT	1.6	67.82	95.67	4.33	64.88
SSRLT	1.8	72.45	96.08	3.92	69.60
SSRLT	2	93.10	96.43	3.57	89.78
SSRLT	2.2	92.43	96.06	3.94	88.79
SSRLT	2.4	91.34	95.85	4.15	87.55
Sol-gel	1	39.33	87.70	12.30	34.49

Note: X = conversion of isopropanol; S_i = selectivity to component i; Y= yield of propene

3.5 Conclusion

A novel method using solid-state reactions at a low temperature (SSRLT) for synthesizing mesoporous chromium phosphates has been developed. The mesoporous chromium phosphates were successfully synthesized in the presence of a surfactant template via a SSRLT route at a low temperature (353 K). This novel method also can be used to synthesize other mesophase metal phosphates. The chromium phosphate synthesized via the SSRLT route exhibits a high specific surface area (250.78 m^2/g) and a narrow pore size distribution after the removal of the surfactant template by heating at 823 K for 6 h. The specific surface area achieved is larger than that obtained via the conventional sol-gel route. In mesoporous chromium phosphate, chromium presents mainly as Cr(III). The walls of the pores of the mesophase have an amorphous structure

and consist of highly-dispersed chromium surrounded octahedrally by phosphates. In the formation of a mesoporous chromium phosphate, the aggregates of the surfactant molecules act as structure-directing templates. The phosphates may interact first with the head groups of the surfactant CTAB, thus stimulating the assembly of chromium ions around the surfactant. The mesoporous chromium phosphate catalyst synthesized via the SSRLT route exhibits a significantly higher catalytic performance in the dehydration of isopropanol to propene, as compared to the amorphous chromium phosphate catalyst synthesized via either the SSRLT or conventional sol-gel routes. Propene selectivity and isopropanol conversion with values as high as 96.43% and 93.10%, respectively, have been achieved over the mesoporous chromium phosphate catalyst synthesized via the SSRLT route from an initial batch with an atomic ratio of P/Cr = 2.0.

4. SYNTHESIS OF MESOPOROUS LITHIUM MANGANESE PHOSPHATES VIA SOLID STATE REACTION AT LOW TEMPERATURE

4.1 Introduction

Recently, Lithium transition-metal (ortho) phosphates have attracted attention as potential Li-ion battery cathode materials due to their lower toxicity, lower cost, and better chemical and thermal stability, when compared to the currently used $LiCoO_2$. In 1996, Goodenough, Akshaya Padhi and coworkers identified lithium iron phosphate ($LiFePO_4$) and other phospho-olivines (lithium metal phosphates with olivine structure) as cathode materials [11]. Because of its low cost, non-toxicity, excellent thermal stability, positive safety characteristics, good electrochemical performance, high specific capacity (170 mA·h/g, or 610 C/g), and the high abundance of iron it gained some market acceptance.

Encouraged by the success of $LiFePO_4$, $LiMnPO_4$ is also attracting increased attention. Lithium manganese phosphate has a redox potential of 4.1 V versus Li^+/Li, which is considered to be the maximum limit accessible to most liquid electrolytes. This is ~0.65 higher than $LiFePO_4$, The high ionic and electronic resistance of $LiMnPO_4$ have rendered it difficult to obtain high electrochemically activity. Li et al. first reported the reversible reaction of Mn(II)↔Mn(III) in olivine phosphate. Their material presented a reversible capacity of ∼140 mA·h g−1 at C/15 within 2.0–4.5 V vs. Li/Li^+. Although several groups have explored various methods to prepare electro-active $LiMnPO_4$, there are very few reports of performance greater than 100 mAh g^{-1} [14, 15].

For the synthesis for $LiMnPO_4$, the formation of olivine structure $LiMnPO_4$ is normally obtained via solid state reaction at high temperature [15, 20 - 24]. Although

scientist cannot obtain ideal materials completely, the high temperature solid state reaction still held a dominant position in the materials synthesis via solid state reaction. Yet these crystalline metal phosphates generally have low specific surface area and small pore volume. Mesoporous phosphate materials have some valuable properties such as high specific surface area and large pore volume, with controllability in nano-pore sizes, framework composition, and particle morphology. Mesoporous lithium manganese phosphates can be synthesized via the sol-gel method and also show an excellent electrochemical performance as a cathode. This technique facilitates the controllable hydrolysis and condensation of precursor species, via the supramolecular assembly of surfactant micelles, generating mesoporous materials with a homogeneous distribution of components at the molecular level.

However, the use of solid-state reactions to synthesize the mesoporous lithium manganese materials at low temperatures has not yet been reported. Here, we present our work on employing solid-state reactions at low temperatures (SSRLT) in the synthesis of mesoporous lithium manganese phosphates. The synthesized mesoporous lithium manganese phosphates have excellent textural properties. Additionally, the electrochemical test of lithium manganese phosphates prepared by SSRLT was performed.

4.2 Overview

The general structure of this chapter includes the preparation of lithium manganese phosphates and lithium iron phosphates via solid state reaction at low temperature their structure and catalytic characterization. Characterization tools include X-ray diffraction, high resolution transmission electron microscopy, and nitrogen adsorption-desorption. The electrochemical test were performed using home designed cells with Lithium foil as the counter electrode, and 1.2M $LiPF_6$ in EC/EMC (3:7 by weight) as the electrolyte, the separator is Celgard 3501 from Celgard Company. The electrochemical property was tested on the Solartron SL1260.

4.2.1 X-ray Diffraction

The structure of the synthesized compounds was determined using X-ray diffraction (XRD) (Brucker D8 advance diffractometer, Cu Kα radiation, wavelength 1.5406 Å). The diffraction data was recorded for 2θ angles between 0.35 and 75°, with a scanning speed of 0.02° /sec.

4.2.2 High Resolution Transmission Electron Microscopy

The morphology of the synthesized compounds was examined using a high resolution transmission electron microscopy (HR-TEM) (JOEM-3010 electron microscope). Energy dispersible X-Ray spectroscopy (EDS) with an elemental analysis accessory (OXFORD) was used to analyze the local composition of the synthesized compounds.

4.2.3 Nitrogen Adsorption-desorption

The BET surface area and porosimetry of the synthesized compounds was measured using the nitrogen adsorption-desorption (Beckman Counter SA 3100). Before adsorption measurements, the specimen was heated from room temperature up to 573 K, evacuated to 10^{-3} Pa, and then kept at that temperature and under vacuum outgasing for 2 h. The specific surface area was determined by the BET method, and the pore size distribution was obtained from the N_2-desorption curve by the BJH (Barrett-Joyner-Halenda) method.

4.2.4 Electrochemical Test

The electrochemical tests were performed using a home designed cell with Lithium foil as the counter electrode, and 1.2M $LiPF_6$ in EC/EMC (3:7 by weight) as the electrolyte, the separator is Celgard 3501 from the Celgard Company. The

electrochemical property was tested on the Solartron SL1260. The charge/discharge rate of the $LiFePO_4$ half cell is 0.1C, between 2.8V to 3.8V. The preparation of the electrode followed these standards: 0.78 g obtained mesoporous $LiMnPO_4$ powder was first mixed with 0.15 g BP2000, then ground for 1 h. Next carbon black is added to increase the electrical conductivity of $LiMnPO_4$.In a separate container, 0.07 g PVDF (Polyvinylidence Fluoride) was dissolved in 1 g NMP (N-Methyl-2-pyrrolidone), and then obtained mixture was mixed vigorously for 0.5 h to get the clear sol. Finally, the obtained NMP sol and the $LiFePO_4$/BP2000 were mixed and grinded for another 0.5 h to obtain the electrode ink. Before coating, the aluminum foil was first washed by acetone. Then the electrode ink would be coated on the aluminum foil by the coater and dried in the oven at 60 ˚C. The effective surface of the electrode would be 10 mg/cm^2.

4.3 Experiment

4.3.1 Objectives

Several samples with different P/Mn ratio were synthesized with solid state reaction at low temperature. The set of samples were accordingly synthesized and characterized with the tools described as to the aforementioned methods and settings.

4.3.2 Synthesis of Mesoporous $LiMnPO_4$ via SSRLT Route

$LiC_2O_3 \cdot 6H_2O$ (Analytical reagent, A.R., Sigma Aldrich), $MnCl_2 \cdot 6H_2O$ (Analytical reagent, A.R., Sigma Aldrich) and $NH_4H_2PO_4 \cdot 2H_2O$ (Analytical reagent, A.R., Sigma Aldrich) in various P/Mn molar ratios were mixed together and ground in a mortar for 20 minutes then mixed further with a selected amount of cetyltrimethyl ammonium bromide (CTAB), and ground together for another 15 minutes. The obtained mixtures with atomic ratios of Li: P: Mn: CTAB = 1.0: x: 1.0: 0.001, where x = 1.0, 2.0 and 3.0, were

transferred into beakers for heating at 373 K for 24 h. After cooling to room temperature, the samples were washed thoroughly with distilled water and then dried at 373 K for 6 h. To remove the surfactant, the specimens were further calcined in N_2 at different temperatures for 6 h. The obtained samples were marked as S_{x-y}, while x equals to the atomic rations of Mn: P and y equals to the calcination temperature. For example, S_{1-600} means the obtained samples was calcined at 600 ˚C, which was with the atomic rations of Mn: P equals to 1:1.

4.4 Results and Discussion

4.4.1 X-ray Diffraction

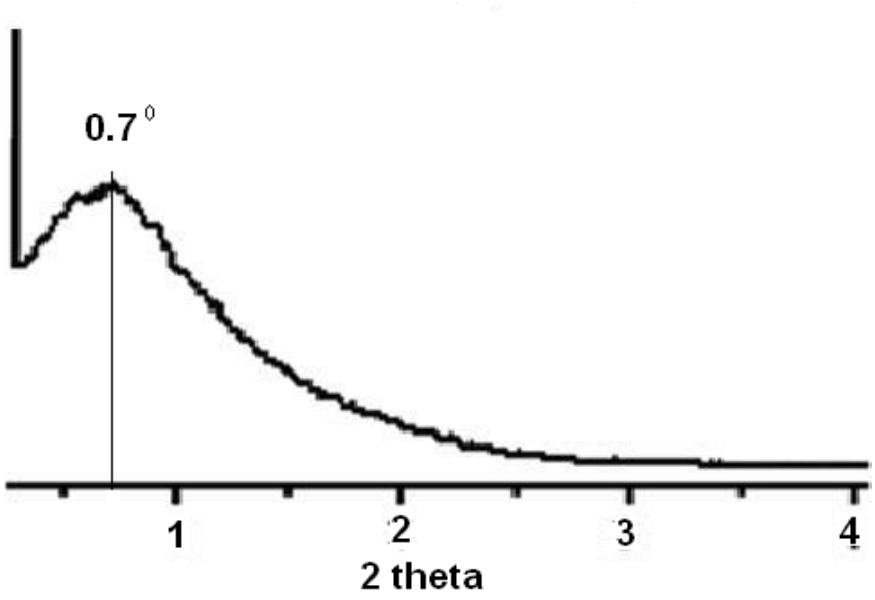

Figure 4.1 XRD pattern for S_{1-600} via solid state reaction

Figure 4.1 shows the XRD pattern of the obtained S_{1-600} via SSRLT method. A peak at $2\theta = 0.70^{o}$ with a d-spacing (pore-to-pore distance) of 12.7 nm present in low angle range ($2\theta = 0.35 - 5^{o}$), indicating that the obtained $LiMnPO_4$ belongs to a

wormhole-like MSU-type structure. No diffraction peak was detected in high angle range, suggesting an amorphous nature associated with the pore walls of this mesoporous material.

4.4.2 HR-TEM Micrograph

As shown in Figure 4.2, the HR-TEM micrograph of a mesoporous lithium manganese phosphate synthesized via the SSRLT shows a very orderly arranged wormhole-like pore array structure, which confirms the presence of a mesophase according to the XRD data.

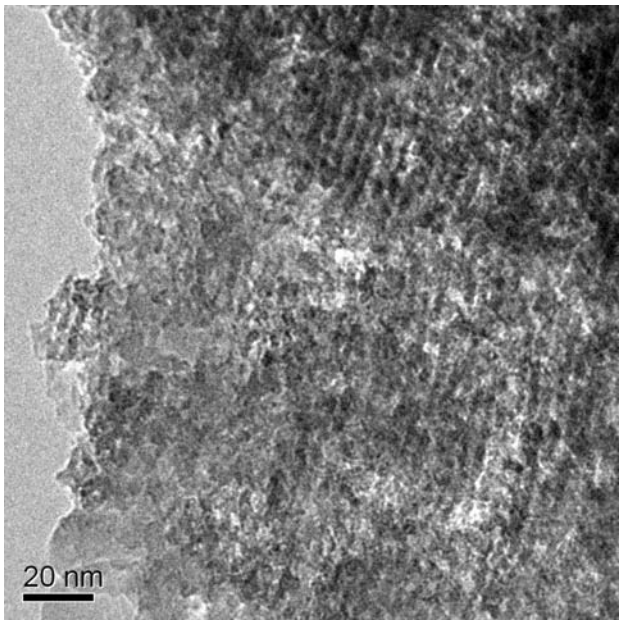

Figure 4.2 The HR-TEM micrograph of the obtained $S_{1\text{-}600}$ via SSRLT method

One possible mechanism for the formation of such a structure is that the surfactant CTAB and lithium manganese phosphate form a uniform and orderly solid array, which consists of rod-like micelles of CTAB surrounded by lithium manganese phosphates. Then a uniform and orderly pore array structure is formed when the rod-like micelles of CTAB are removed from this solid array through calcinations. Thus, the

surfactant CTAB plays an important role in the pore structure of lithium manganese phosphates. In addition, the mesopores exhibit mostly wormhole-like pore geometry, with the average distance between the centers of the wormhole-like pores of ca. 3.8 nm, which correlates well with the results from the XRD data.

4.4.3 SEM Micrograph

Figure 4.3 shows the SEM micrograph of the mesoporous $LiMnPO_4$, which indicates mainly a spherical morphology and a particle size of about 200 nm. It hints that the formation of the mesoporous $LiMnPO_4$ had been a result of supramolar assembly process.

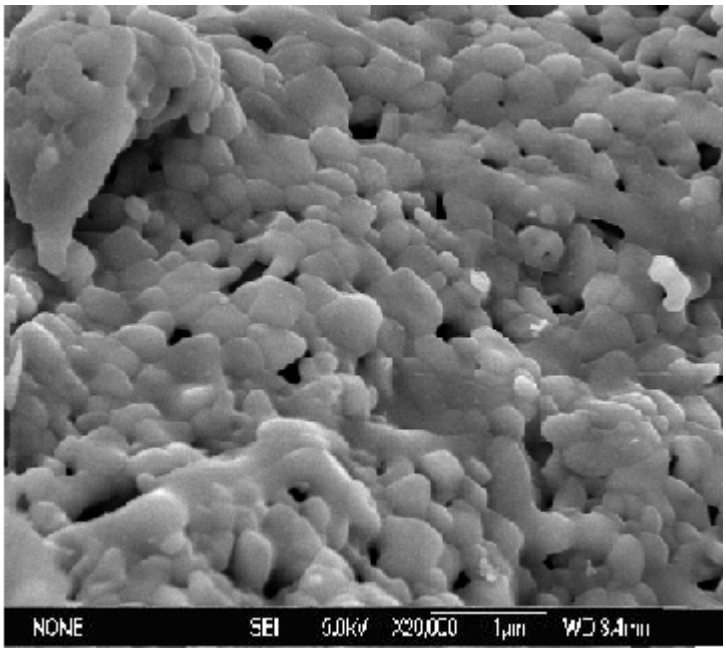

Figure 4.3 The SEM micrograph of the obtained $S_{1\text{-}600}$ via SSRLT method

Table 4.1 EDS results and d-Spacings in Å obtained from XRD spectra

	Mn/P in the initial batches		
	1/1	1/2	1/3
Mn/P in the specimens	0.98/1	1/1.18	1/1.20
O/P in the specimens	3.78	4.23	3.89
d-spacing of the specimens	3.8	4.13	5.17

The Li/Mn/P and O/P atomic ratios in the lithium manganese phosphates synthesized via the SSRLT route were determined using EDS. All results are listed in Table 4.1. The results show that the Li/Mn/P atomic ratios in the synthesized specimens are approximately equal to 1:1:1, no matter how much was those in the initial batches, and the O/P atomic ratios are around 4.

4.4.4 BET Results

The nitrogen adsorption-desorption isotherm and the pore size distribution curve (in the inset) of the mesoporous lithium manganese phosphate $S_{1\text{-}600}$ synthesized via the SSRLT route are shown in Figure 4.4.

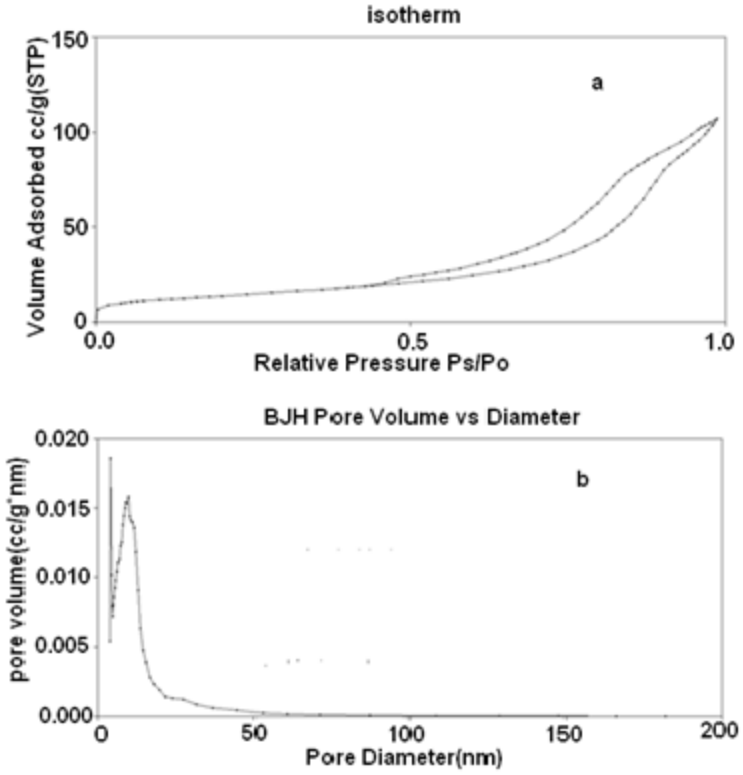

Figure 4.4 The nitrogen adsorption-desorption isotherm and pore size distribution curve of $S_{1\text{-}600}$

The isotherm can be ascribed to type IV in the IUPAC classification and indicates a typical mesostructure. The desorption hysteresis loop corresponds to type H2, and is caused by pore blocking effects during desorption, indicating an ink-bottle pore geometry of the mesostructure. The BET specific surface area is 133.76 m^2/g and the pore volume is 0.2987 cm^3/g, these were calculated based on the adsorption in the relative pressure ranging from 0.05 to 0.2 and the relative pressure of 0.9814, respectively. The mesoporous lithium manganese phosphate has a uniform and narrow pore size distribution, with most of the pore sizes centering around 4.8 nm. It can be found that the specific surface area and pore volume are ca. 0.4 - 0.5 nm fold and the pore size ca. 0.19 nm. This suggests that the SSRLT is effective in increasing the thickness of pore walls, which is useful to the stability of mesoporous materials.

Table 4.2 BET results for $LiMnPO_4$ with different ratio and calcined temperature

Sample $LiMnPO_4$	Structure type	Surface area (m^2/g)
$S_{1\text{-}400}$（Li:Mn:P=1:1:1)	Amorphous	198.21
$S_{1\text{-}500}$（Li:Mn:P=1:1:1)	Mesoporous	256.63
$S_{1\text{-}600}$（Li:Mn:P=1:1:1)	Microporous &Mesoporous	133.76
$S_{2\text{-}600}$ (Li:Mn:P=1:1:2)	Mesoporous	98.15
$S_{3\text{-}600}$ (Li:Mn:P=1:1:3)	Mesoporous	112.75

The BET results for the obtained $LiMnPO_4$ with different ratio and calcined temperature have also been shown as in the table 4.2. It can be shown that the obtained $LiMnPO_4$ at 400 ˚C is not an olivine or mesoporous structure but in fact amorphous structure, yet the surface area can be as high as 198.21 m^2/g. And when the calcined temperature was increased to 500 ˚C, the $LiMnPO_4$ possessed a mesoporous structure and the surface area was as high as 256.63 m^2/g. When the calcined temperature was increased to 600 ˚C, the obtained $LiMnPO_4$ started to crystallize, and yet it showed a microporous and mesoporous structure. Yet the surface area decreased to 133.76 m^2/g.

4.4.5 Electrochemical Test Results--Effect of Calcined Temperature

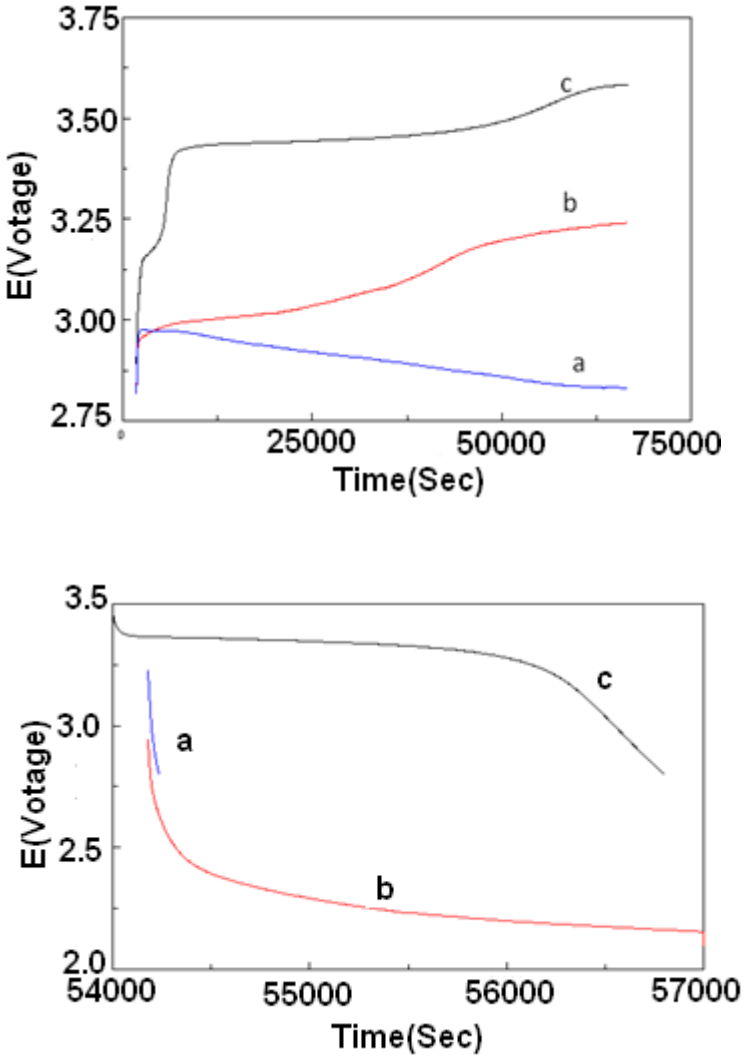

Figure 4.5 The initial charge/discharge curve of $LiMnPO_4$ which calcined at different temperature.(cycled in the voltage of 2.8 V to 3.8 V at 0.1 C.)

Figure 4.5 shows the charge curve of mesoprous $LiMnPO_4$ calcined at different temperatures. It can be seen that the calcined temperature greatly affects the capacity of the $LiMnPO_4$ synthesized by solid state reaction. The sample calcined at 400 ˚C shows the worst electrochemical property, when it was charged, the potential dropped quickly. When the calcined temperature was increased to 500˚C, the charge voltage increased to 3.25V. When the calcined temperature was increased to 600˚C, the charge voltage increased to 3.60 V while the first time discharge capacity was seen to be as high as 100

mAh/g. Obviously, the capacity of $LiMnPO_4$ is greatly affected by the calcined temperature. It is probably due to the different $LiMnPO_4$ structures that were formed under different calcined temperatures. Normally, the crystallinity of the obtained $LiMnPO_4$ at 400 ˚C is not good enough; it is not an olivine structure, or mesoporous structure but actually an amorphous structure. And when the calcined temperature was increased to 500 ˚C, the $LiMnPO_4$ started to crystallize though it still possessed a mesoporous structure. And when the calcined temperature was increased to 600 ˚C, it is assumed that part of the crystalline structure had formed, which could be supported by the BET and XRD results.

4.4.6 Electrochemical Test Results--Effect of Different P:Mn Ratio

The charge/discharge curve of $LiMnPO_4$ with different P/Mn ratio is been shown in Figure 4.6. Also the charge/discharge capacity of $LiMnPO_4$ with different P/Mn ratio is shown in Table 4.3. It can be seen from the results that P/Mn ratio is not the main determinant of the electrochemical property of the synthesized $LiMnPO_4$, the capacity of the $LiMnPO_4$ with different P: Mn ratio is almost the same, varying from 98 to 113 mAh/g. This result is accordant to the EDX results, which show that the Li/Mn/P atomic ratios in the synthesized specimens are approximately equal to 1:1:1, no matter the ratio in the initial batches, and the O/P atomic ratios are around 4.

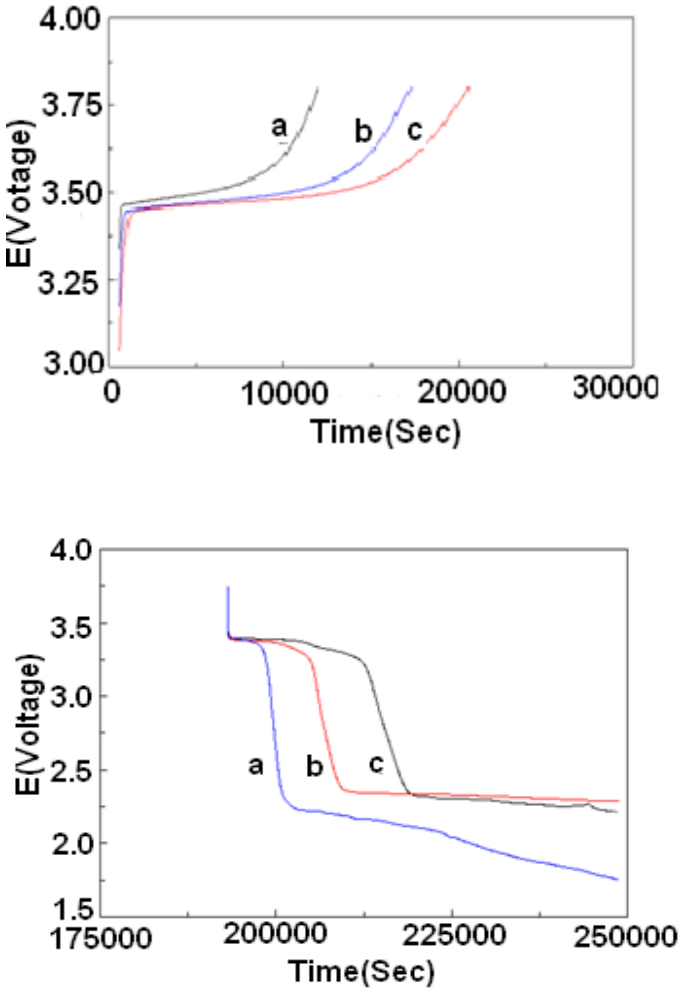

Figure 4.6 The charge/discharge curve of $LiMnPO_4$ calcined at 600 ˚C, a.1:1; b.1:2; c.1:3; (The test cycled in the voltage of 2.8 V to 3.8 V at 0.1 C)

Table 4.3 The charge/discharge capacity of the $LiMnPO_4$ calcined at 600 ˚C

P:Mn ratio	1:01	1:02	1:03
charge capacity	98	110	113
discharge capacity	83	90	95

4.5 Conclusion

A novel method using solid-state reactions at a low temperature (SSRLT) for synthesizing mesoporous lithium manganese phosphates has been developed. The mesoporous lithium manganese phosphates were successfully synthesized in the presence of a surfactant template via a SSRLT route at a low temperature (353 K). This novel method can also be used to synthesize other mesophase metal phosphates. The lithium manganese phosphates synthesized via the SSRLT route exhibit a high specific surface area (256.63 m^2/g) and a narrow pore size distribution after the removal of the surfactant template by heating at 873 K for 6 h. The structure can be controlled by the calcined temperature. When the calcined temperature was increased to 600 ˚C, the obtained $LiMnPO_4$ started to crystallize. The obtained $LiMnPO_4$ shows a microporous and mesoporous structure. The surface area decreased to 133.76 m^2/g. Electrochemical tests of li-ion batteries have also been performed. The results show that when obtained mesoporous $LiMnPO_4$ is calcined at 600 ˚C, the charge voltage increased to 3.60 V while the first time discharge capacity was as high as 100 mAh/g.

5. MECHANISM STUDY FOR THE MESOPOROUS PHOSPHATE SYNTHESIS VIA SOLID STATE REACTION

5.1 Introduction

At this time a volumous amount of work has been done to synthesize different mesoporous materials. From the initial M41S mesoporous materials to FSM, HMS, MSU, SBA, KIT *et al.*, there have been literally thousands of publications dealing with mesoporous ceramics, with a wide variety of synthetic methods being developed. And also, many research teams have focused on the understanding of the formation mechanisms. However, most of the proposed mechanisms concern silica-based MCM-41 type solids. Meanwhile, a lot of different modes of synthesis have been rapidly extended to non-siliceous mesoporous. And all of modes are based on the same point which is that the template has play an important role in the formation of mesoporous materials, though the formation mechanism of mesoporous materials still remains arguable.

In this text, we present our work on employing the solid-state reactions at low temperature (SSRLT) in synthesis of mesoporous chromium phosphates. And for the first time, we have focused on the understanding of the formation mechanism of mesoporous chromium phosphates by using FITR method. The results show that the CTAB do play an important role in the formation of mesoporous chromium.

5.2 Overview

In this chapter, the mechanism for the formation of mesoporous phosphate via solid state reaction has been studied via Fourier transform infrared (FT-IR) spectroscopy. Basically, the formation of CTAB micelles was examined using Fourier transform

infrared (FT-IR) spectroscopy (Varian 3100 spectrometer with a DTGS detector and a CeI beamsplitter). Before the measurement, the sample was ground together with KBr and pressed into a wafer. The data ranging from 300 cm^{-1} to 4000 cm^{-1} were recorded as accumulated results of 20 scans, at a resolution of 4 cm^{-1}.

5.3 Experiment

5.3.1 Synthesis of Mesoporous $CrPO_4$ via SSRLT Route

$CrCl_3 \cdot 6H_2O$ (Analytical reagent, A.R., Sigma Aldrich) and $NaH_2PO_4 \cdot 2H_2O$ (Analytical reagent, A.R., Sigma Aldrich) were mixed together and grinded in a mortar for 20 minutes, and then mixed further with a selected amount of cetyltrimethyl ammonium bromide (CTAB) and grinded together for another 15 minutes. The obtained mixtures with atomic ratios of P: Cr: CTAB = 2.0: 1.0: 0.001, were transferred into beakers for heating at 373 K for 24 h. After cooling to room temperature, the samples were washed thoroughly with distilled water and then dried at 373 K for 24 h. To remove the surfactant, the specimens were further calcined in N_2 at 823 K for 6 h.

5.4 Results and Discussion

5.4.1 The FT-IR Spectra of CTAB and $CrPO_4$(P/Cr = 2)

The FT-IR spectra of CTAB and mesoporous chromium phosphate synthesized via the SSRLT route (with P/Cr atomic ratio = 2 and removed CBAT surfactant) is shown in Figure 5.1. The spectrum of the pure surfactant CTAB (Figure 5.1 a) exhibits the characteristic vibration absorptions of a quaternary ammonium compound with a long alkyl chain, i.e., $\nu(CH_3)$ and $\nu(CH_2)$ (3020, 2920, and 2850 cm^{-1}), $\delta(CH_3)$ and $\delta(CH_2)$

(1480~1360 cm^{-1}), ν(C-N) (1290 and 1240 cm^{-1}), ν_{as}(N-R_4) (~960 cm^{-1}), γ(CH_2) (730 cm^{-1}), and ν_s(N-R_4) (~720 cm^{-1}). With the exception of the band at 2347 cm^{-1} ($\nu_{as}(CO_2)$) [37], the weak bands in the range between 2650 and 1600 cm^{-1} probably reflect combinations or overtones of the skeleton of CTAB. In the spectrum of mesoporous chromium phosphate containing the CTAB (Figure 5.1 b), some of the characteristic vibration bands of CTAB (2920, 2850, 1480, 1290, 910 and 715 cm^{-1}) are present. Besides several broad bands centered at 3500 cm^{-1} (ν(OH or H_3O^+) [38 – 39], and/or ν(P-OH), those at 1630 cm^{-1} (δ_{as}(OH or H_3O^+) [39], 1070 cm^{-1} ($\nu_s(PO_4)$) [26], and 505 cm^{-1} (δ_{out}(POH) and/or δ(PO_4) are also detected [39]. Compared to Figure 5.1 a, the intensities of the absorption bands of both the alkyls and the N-R_4 head group in the CTAB in Figure 5.1 b are much smaller, especially for the N-R_4 head group. The wave numbers of the absorption bands of the N-R_4 head group shifted from 960 and 720 cm^{-1} in Figure 5.1 a to 910 and 715 cm^{-1} in Figure 5.1 b, respectively. These results indicate that the CTAB has been incorporated into the mesopores of the chromium phosphate, and there is a strong interaction between the head group of the CTAB and the chromium phosphate moieties, which contributes to the building of the mesoporous chromium phosphate. In the spectrum of mesoporous chromium phosphate after the CTAB removal (Figure 5.1 c), all the bands of CTAB disappeared but those of phosphates (shown in Figure 5.1 b) remained. Two new bands (930 and 755 cm^{-1}) appeared (Figure 5.1 c), due to the mixed motions involving both the PO_4 tetrahedron and the CrO_6 octahedron [27]. The characteristic vibrations due to the skeleton of PO_4 ($\nu_s(PO_4)$ and δ(PO_4)) have been shifted from 1070 and 505 cm^{-1} for the specimen containing the surfactant CTAB to 1130 and 530 cm^{-1} for the specimen without the surfactant CTAB. This indicates that, in the formation of mesoporous chromium phosphates, the phosphates play an important role by interacting first with the surfactant CTAB, thus stimulating the assembly of chromium ions around the surfactant molecules. There is a stronger interaction between chromium and phosphate ions after the surfactant removal.

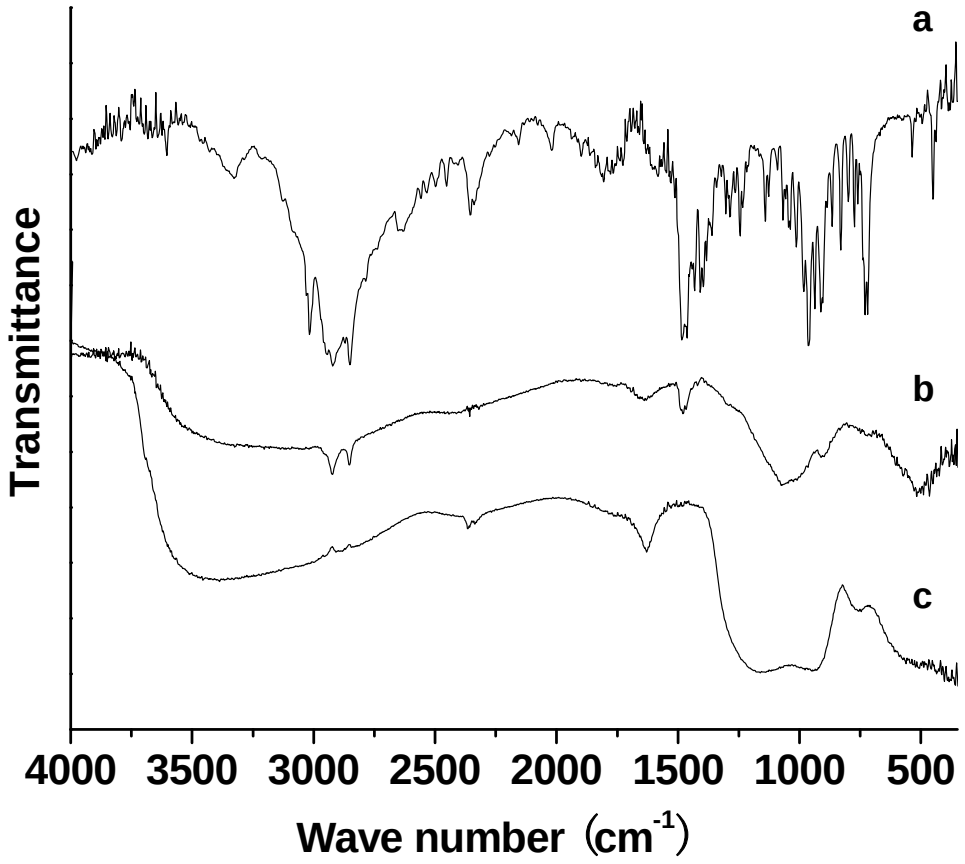

Figure 5.1 FT-IR spectra of pure CTAB (a) and mesoporous chromium phosphate prepared (P/Cr = 2.0) before (b) and after (c) the surfactant removal

5.4.2 FT-IR Spectra of $CrPO_4$ before Surfactant Removal

Figure 5.2 is the FT-IR spectra of chromium phosphate specimens prepared from initial batches with various P/Cr atomic ratios, before the surfactant removal. For P/Cr ≥ 2.0 (Figure 5.2 d - g), the spectra are very similar to each other and the vibration band assignment is similar to that of P/Cr = 2.0 in Figure 5.2 b. The spectrum for P/Cr = 1.8 (Figure 5.2 c) is similar to that of P/Cr ≥ 2.0, but the intensity of the band at 2347 cm^{-1} ($\nu_{as}(CO_2)$) is much larger in the former than in the latter. For P/Cr < 1.8 (Figure 5.2 a and b), most of the vibration bands observed for P/Cr = 1.8 in Figure 5.2 c are nearly unchanged, except that the vibration bands of CTAB are absent.

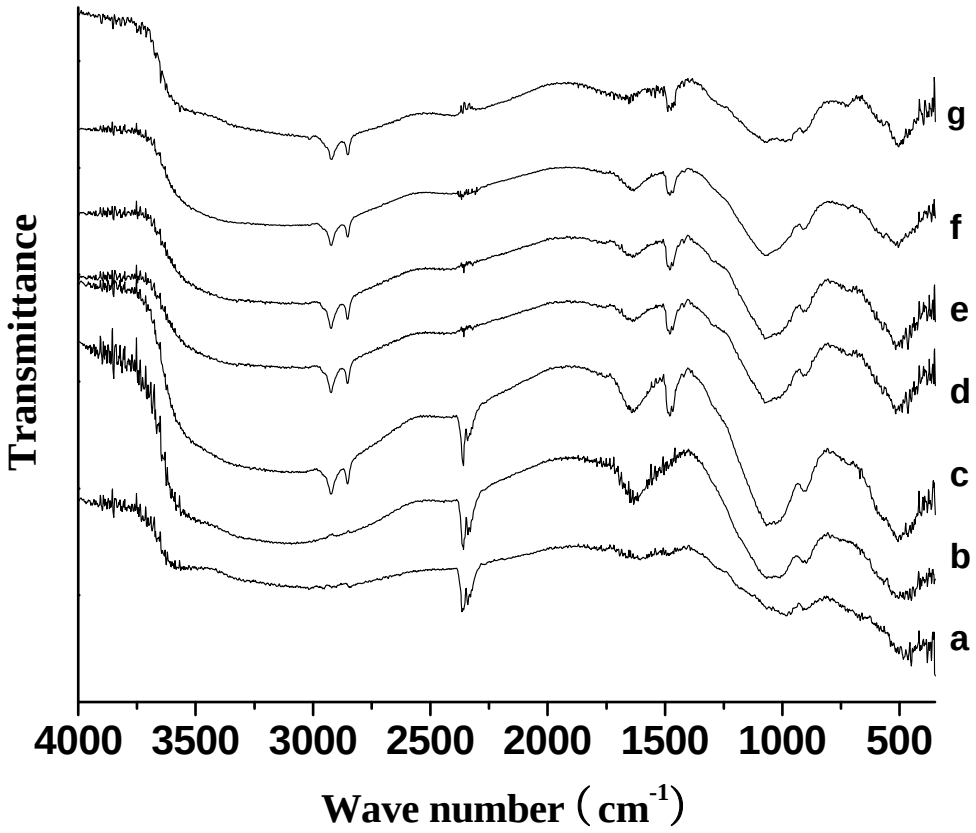

Figure 5.2 FT-IR spectra of mesoporous chromium phosphate prepared with various P/Cr atomic ratios before the surfactant removal. The P/Cr atomic ratio is equal to a) 1.0, b) 1.6, c) 1.8, d) 2.0, e) 2.2, f) 2.4, and g) 3.0.

5.4.3 FT-IR Spectra of $CrPO_4$ after Surfactant Removal

Figure 5.3 presents the FT-IR spectra of chromium phosphate specimens prepared from initial batches with various P/Cr molar ratios after the surfactant removal. The spectra are similar to those of Figure 6 c, however, the intensity of the band at 2347 cm^{-1} ($\nu_{as}(CO_2)$) is obviously larger for P/Cr $\leq$ 1.8 (Figure 5.3 a - c) than for P/Cr > 1.8 (Figure 5.3 d - g).

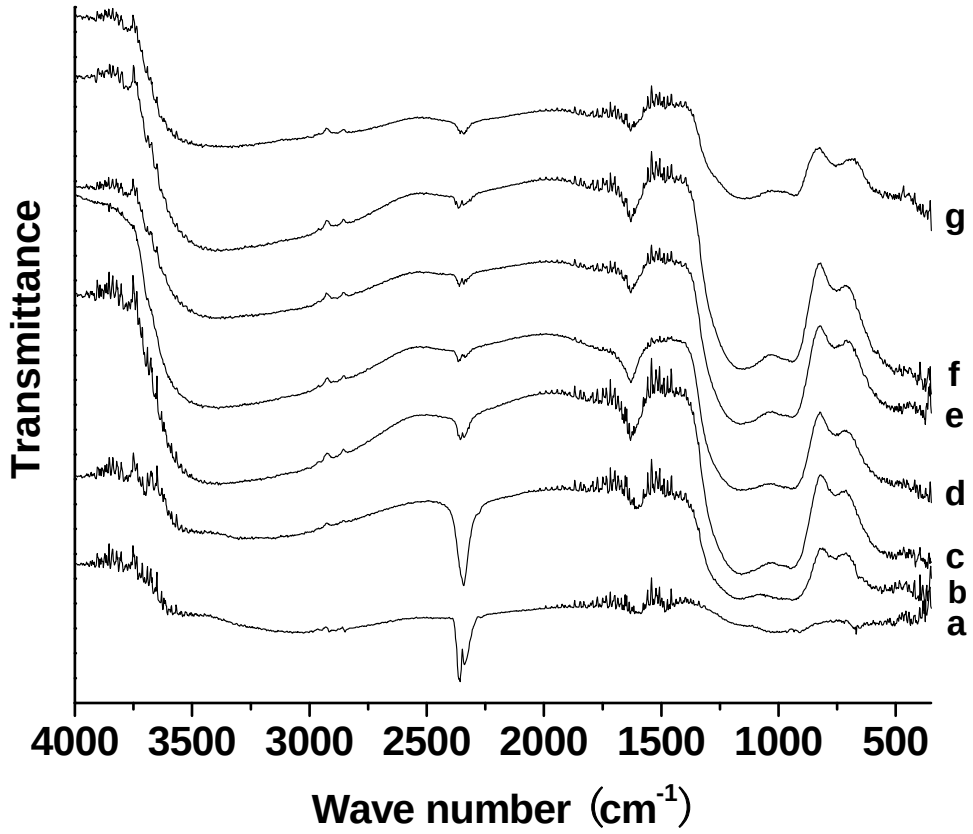

Figure 5.3 FT-IR spectra of mesoporous chromium phosphate prepared with various P/Cr atomic ratios after the surfactant removal. The P/Cr atomic ratio is equal to a) 1.0, b) 1.8, c) 2.0, d) 2.0, e) 2.2; f) 2.4, and g) 3.0

5.4.4 Formation Mechanism of Mesoporous $CrPO_4$ via SSRLT

So far, many research teams have focused on the understanding of the formation mechanisms. However, most of the proposed mechanisms concern silica-based MCM-41 type solids. Meanwhile, a lot of different modes of synthesis have been rapidly extended to non-siliceous mesoporous. And all of modes are based on the same point which is that the template has play a important role in the formation of mesoporous materials, though the formation mechanism of mesoporous materials still remains arguable. Two famous models are liquid-crystal templating mechanism and charge density matching mechanism.

About the formation mechanism of MCM-41 mesoporous materials, the scientists from Mobil firstly reported the liquid-crystal templating mechanism. From this mechanism, they believe that the liquid-crystal surfactant is just the template for the MCM-41 structure formation. And there are two possible synthesis procedures for the formation of MCM-41 [3]. In this mechanism, inorganic materials firstly occupy the continuous solvent (water) region to create inorganic walls between the surfactants cylinders. It may be that encapsulation occurs because anionic aluminosilicate species enter the solvent region to balance the cationic hydrophilic surfaces of the micelles. Then it might be the introduction of the aluminosilicate species themselves that mediates the hexagonal ordering. 2) Once the ordered array is established, a stable mesoporous molecular sieve is formed after the removal of the organic material. However, later results show that the mesoporous materials could also formed even the density of the templates is lower than that needed for the formation of liquid-crystal. For example, for the Cetyltrimethylammonium bromide (CTAB), hexagonal ordering could be formed when the density of surfactants reaches 28%, while for the formation of cubic ordering, the density of surfactants should be as high as 60%. However, MCM-41 mesoporous materials could be obtained even the density of surfactants is as low as 2%. And MCM-48 (which has a cubic structure) could be obtained when the density of the surfactants is as low as 10%. So, under some way, this mechanism is not so reasonable.

Just as stated in the above, Monnier *et al*. [40] reported that MCM-41 could be prepared even at the density of surfactants is as low as 2% during which the micelles could be formed, or at a higher temperature (>70 ℃) which obtained micelles is not stable. During the water-CTAB system, when the density of CTAB is lower than 5%, there are only micelles, however, the mesoporous materials could also be formed when mixing the aluminosilicate species and CTAB together. Based on the experiment, Monnier reported the charge density matching mechanism and three processes are identified: multidentate binding of silicate oligomers to cationic surfactant, preferential silicate polymerization in the interface region, and charge density matching between the

surfactant and silicate. In order to reach this charge density balance, a lamellar structure begins to transfer to hexagonal or cubic mesostructures.

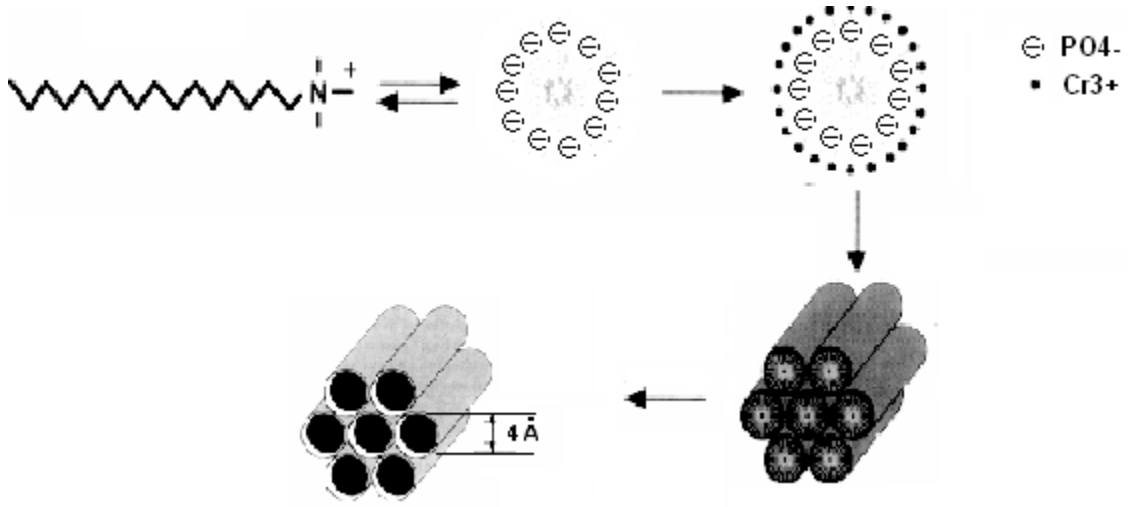

Figure 5.4 The formation mechanism for the synthesis of mesoporous chromium phosphate.

Here, in our experiment, the above FT-IR spectra (Figure 5.1, 5.2 and 5.3) show that no CTAB was incorporated into the chromium phosphate, when the specimens were prepared from initial batches with atomic ratios of P/Cr < 1.8. In the XRD characterization of these specimens, we found that chromium phosphate mesophases are formed only for atomic ratios P/Cr $\geq$ 1.8 (see Figure 3.1). Therefore, the surfactant CTAB plays a key role in the formation of the mesoporous chromium phosphate. It probably involves the formation of mesoporous chromium phosphate by first assembling the phosphates around the head groups of the surfactant CTAB and subsequently assembling chromium around the moiety of the CTAB and the phosphates. The removal of the surfactant promotes the interaction between phosphate and chromium ions, resulting in the formation of chromium phosphate. The higher P/Cr atomic ratios (> 1.8) facilitate the interactions of the CTAB and the phosphates, which in turn, results in the incorporation of the surfactant CTAB into the chromium phosphates. Another result of the higher atomic ratios of P/Cr (> 1.8) is that the chromium is surrounded by a larger number of phosphates, thus, the adsorption of CO_2 over chromium is largely hindered, which is in contrast to the case with lower atomic ratios of P/Cr (< 1.8). This is evidenced

by the larger intensity of the CO_2 vibration bands for P/Cr < 1.8 than for P/Cr > 1.8 (cf. Figure 3.2 a - c and d - g; Figure 3.3 a - c and d - g).

5.5 Conclusion

The mesoporous chromium phosphates were successfully synthesized in the presence of a surfactant template via a solid state reaction at a low temperature (353 K). The formation of the mesoporous chromium phosphate has been developed by using the FTIR.In the formation of a mesoporous chromium phosphate, the aggregates of the surfactant molecules act as structure-directing templates. The phosphates may interact first with the head groups of the surfactant CTAB, thus stimulating the assembly of chromium ions around the surfactant. It probably involves the formation of mesoporous chromium phosphate by first assembling the phosphates around the head groups of the surfactant CTAB and subsequently assembling chromium around the moiety of the CTAB and the phosphates. The removal of the surfactant promotes the interaction between phosphate and chromium ions, resulting in the formation of chromium phosphate.

6. PREPARATION OF HIGHLY POROUS METAL ORGANIC FRAMWORK(MOFS) COMPLEX FOR CARBON DIOXIDE STORAGE

6.1 Overview

Coal-fired power plants currently generate approximately 50% of the electricity in the United States. While coal is a cheap and abundant resource, the continued reliance upon coal as an energy source could potentially have serious consequences in terms of global warming. Capturing carbon dioxide from coal-fired power plants, thereby preventing release into the atmosphere is of fundamental importance. Effective systems for CO_2 removal must combine high selectivity and capacity with minimal energetic input to liberate the captured CO_2. Materials presently used are amine solutions, zeolites, and porous membranes, but all fall short in one or more of these categories [41 - 44].

Metal-Organic Frameworks are crystalline compounds consisting of metal ions or clusters coordinated to often rigid organic molecules to form one-, two-, or three-dimensional structures that can be porous [45 - 46]. In some cases, the pores are stable after the elimination of the guest molecules (often solvents) and can be used for the storage of gases such as hydrogen and carbon dioxide. To date, several MOFs have been shown to exhibit exceptional CO_2 storage capacity under equilibrium conditions where pure CO_2 or gas mixture is introduced into the pores [47 - 50].

Many researchers have found that the introduction of functional groups to the structure of MOFs could greatly increase the CO_2 storage capacity. In this text, by employing a bi-dentate ligand 5-nitroisophthalic acid, we synthesized a copper based metal organic polyhedron, which is considered as a miniature MOF, with a formula of $Cu_{24}(\text{nitro-IPA})_{24}(DMF)_n$.(nitro-IPA = 5-nitroisophthalic acid; DMF =

dimethylformamide). And also, the Nitro-MOFs have also been obtained by introduction of Nitro to the structure.

The general structure of this chapter includes the preparation of Nitro-MOFs and their structure and CO_2 storage capacity characterization. Characterization tools include Single-crystal X-ray diffraction, Scanning electron microscopy (SEM). To evaluate the storage capacity performance of the synthesized MOFs, a home-made storage apparatus has been designed.

6.1.1 Synchrotron X-ray Radiation at ChemMatCARS Beamlines

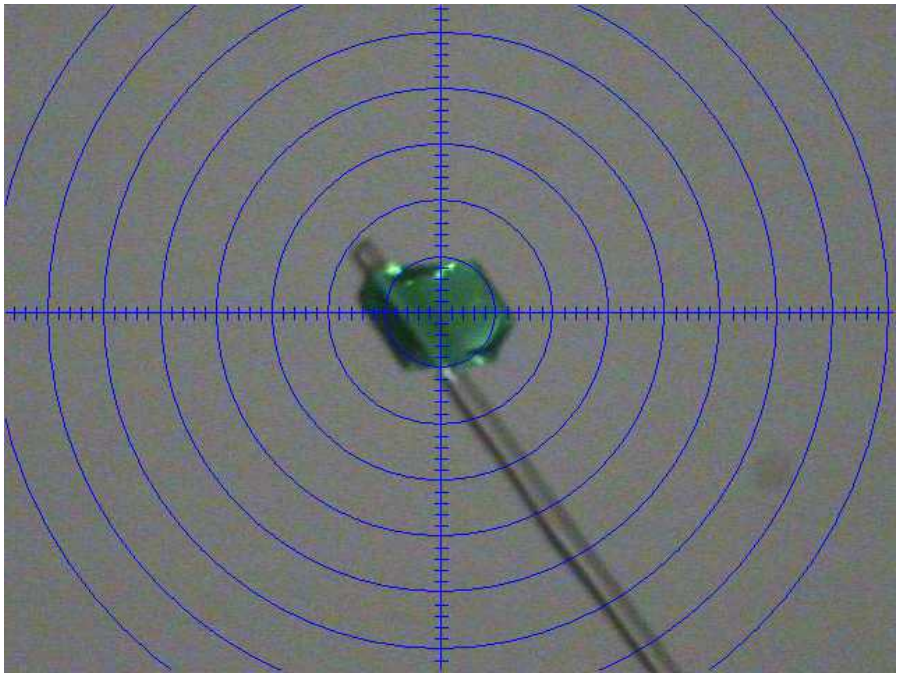

Figure 6.1 The green block was placed onto the trip of a 0.1mm diameter glass fiber

Due to the weakly diffracting nature of the crystal, the diffraction data were acquired with synchrotron X-ray radiation at ChemMatCARS beamline, Advanced

Photon Source, Argonne National Laboratory. A green block (approximate dimensions $0.10 \times 0.07 \times 0.04$ mm^3) was placed onto the tip of a 0.1 mm diameter glass fiber and mounted on a platform diffractometer equipped with an APEX II detector at 120(2) K.

6.1.1.1 Data Collection

The data collection was carried out using synchrotron X-ray radiation (λ = 0.41328 Å, diamond 111 monochromator) swith a frame time of 0.5 second and a detector distance of 7.0 cm. Two major sections of frames were collected with 0.5º stepsize in ϕ and a detector position of -5° in 2θ. Data to a resolution of 0.80 Å were considered in the reduction. Final cell constants were calculated from the xyz centroids of 1255 strong reflections from the actual data collection after integration (SAINT).1.The intensity data were corrected for absorption (SADABS).2. Please refer to Table 6.1 for additional crystal and refinement information.

6.1.1.2 Structure Solution and Refinement

The space group P-1 was determined based on intensity statistics and systematic absences. The structure was solved and refined using SHELXTL.3. A direct methods solution was calculated, which provided most atomic positions from the E-map. Full-matrix least squares / difference Fourier cycles refined with anisotropic displacement parameters. The hydrogen atoms were placed in ideal positions and refined as riding atoms with relative isotropic displacement parameters. Approximately 46% of the unit cell volume comprises a large region of disordered DMF solvents which could not be modeled as discrete atomic sites. PLATON/SQUEEZE 4 was employed to calculate the contribution to the diffraction from the solvent region, and it estimated a total count of 391 electrons per unit cell which could be assigned as 10 DMF molecules. Using a set of solvent-free diffraction intensities, the final full matrix least squares refinement converged to R1 = 0.0646 and wR2 = 0.1438 (F2, all data). The remaining electron density is minuscule and located on bonds.

6.1.2 Nitrogen Adsorption and Desorption

The BET surface area and porosimetry of the synthesized compounds were measured using nitrogen adsorption-desorption (Beckman Counter SA 3100). Before adsorption measurements, the specimen was heated from room temperature up to 573 K, evacuated to 10^{-3} Pa, and then kept at that temperature and under that vacuum outgasing for 2 h. The specific surface area was determined by the BET method, and the pore size distribution was obtained from the N_2-desorption curve by the BJH (Barrett-Joyner-Halenda) method.

6.1.3 Determine the CO_2 Capacity of MOF Complexes

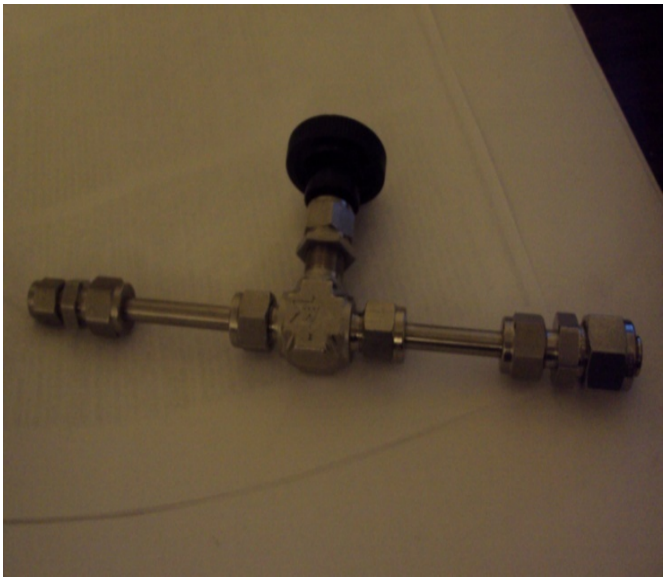

Figure 6.2 The sample holder for the CO_2 capacity of the MOF complexes.

The CO_2 absorption on the MOF complexes surface will be examined as in the following, the absorption of pure carbon dioxide will be investigated. Briefly, certain amount of activated MOFs (solvent molecules removed under vacuum) will be placed in

a stainless steel vessel. The vessel is sealed and weighed using an analytical balance. Ultra-pure carbon dioxide is then introduced into the vessel under various pressures to saturate the MOF complexes. The vessel is then sealed and weighed again. The weight increase observed will correspond to the amount of carbon dioxide absorbed at the surface of the MOF complexes.

To confirm the weight gain is due to the absorption of CO_2, the vessel will be subsequently heated to 200 ˚C to allow the release of the adsorbed gas. Any gas released will be guided into a $Ba(OH)_2$ solution. CO_2 readily reacts with $Ba(OH)_2$ to yield $BaCO_3$ as a white precipitate, which will be collected, washed by water, dried under vacuum and weighed to determine the amount of CO_2 generated.

6.2 Experiment

6.2.1 Preparation of Copper Based Metal Organic Polyhedral

The Cu-MOF complexes are going to be synthesized via a conventional thermal reaction (Figure 6.3) [51]. Briefly, 50 mM copper(II) nitrate solution in DMF is added to an equal amount of isophthalic acid or its derivatives dissolved in DMF as well. The resulting solution is heated at 80 ˚C for 12 hours. The correspondent copper-MOF complexes formed will precipitate out as microcrystals due to the much reduced solubilities of these macromolecules.

6.2.2 Preparation of (Nitro-) copper Based Metal Organic Frameworks

The Nitro-Cu-MOF complexes are going to be synthesized via a conventional thermal reaction (Figure 6.3) [51]. Briefly, 50 mM copper (II) nitrate solution in DMF is added to an equal amount of nitro-isophthalic acid or its derivatives dissolved in DMF as well. The resulting solution is heated at 80 ˚C for 12 hours. The correspondent nitro-Cu-

MOF complexes formed will precipitate out as microcrystals due to the much reduced solubilities of these macromolecules.

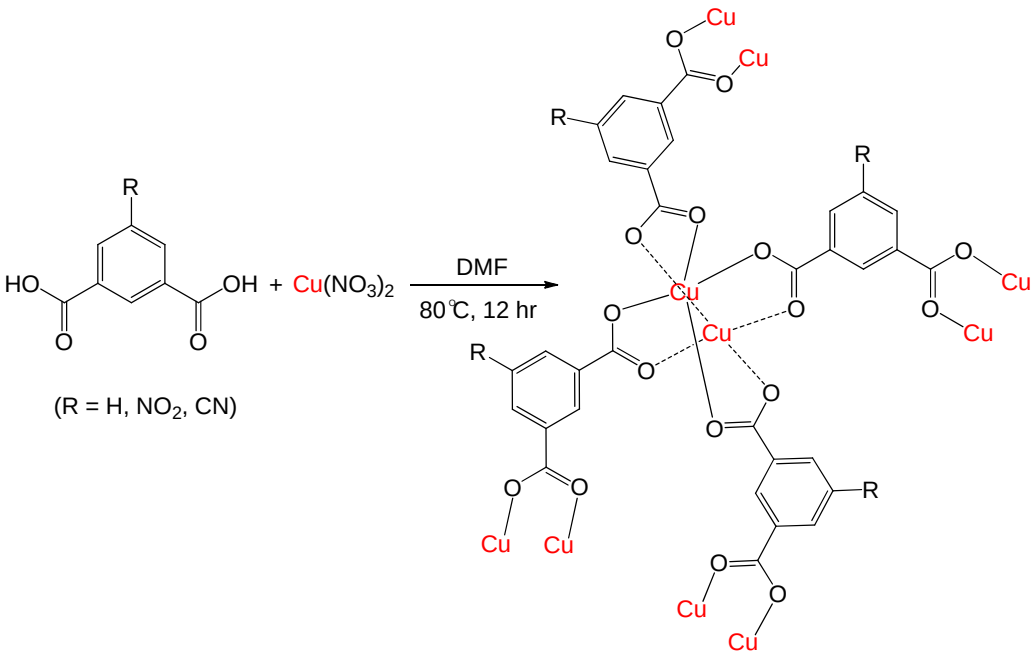

Figure 6.3 Preparation of the nitro-copper based metal organic frameworks.

6.3 Results and Discussion

6.3.1 Structure Analysis for Cu-MOFs

It could be shown from the figure 6.4, the arrangement results in a porous polyhedron could be described in the following: it results in a porous polyhedron having 8 triangular and 6 square crevices that are 8 and 12 Å across, respectively, and a benzene unit depth (Figure 6.4 a, c). These open into an internal spherical cavity having an average diameter of 15 Å and a volume of 1766 $Å^3$. Each paddle-wheel unit of the Cu-O-C polyhedron has two terminal ligands: one pointing into the internal cavity toward the center of the polyhedron while the other is bound to the copper center outside pointing away from the outside surface of the polyhedron. Thus, the paddle-wheel units have a

total of 24 terminal DMF and water ligands. These are distributed as follows: 4 units have only DMF (8 DMF), 6 units have 1:1 DMF: water (6 DMF and 6 water), and 2 units have only water ligands (4 water). A combination of 8 DMF and 4 water ligands point toward the center of the polyhedron, while additional 6 DMF and 6 water ligands point away from the surface of the polyhedron to give it an overall size of 34 Å (with terminal ligands) or 25 Å (without terminal ligands) in diameter.

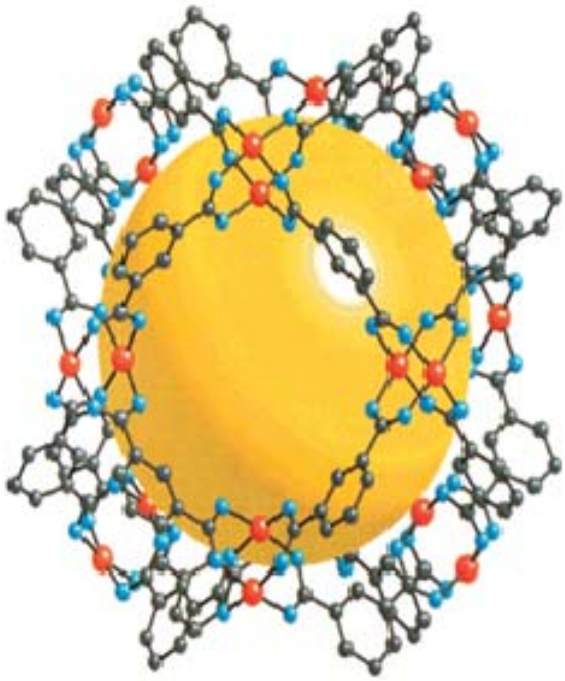

Figure 6.4 Formation of Cu-MOF complex. The crystal structure of Cu-MOF (when R = H) showing copper coordination spheres (Cu, red; O, blue, C; gray) [50]

6.3.2 Structure Analysis for Nitro-Cu-MOFs

The secondary building unit(SBU) for the obtained Nitro-Cu-MOFs could be shown in Figure 6.5, expanded to show the four 5-nbdc ligands, each coordinated to a dicopper paddle wheel unit via one of their carboxylate groups. The second carboxylate group of each 5-nbdc ligand coordinates to another paddle wheel unit, generating the

extended structure. As well, both of the independent copper centers and both of the independent 5-nbdc ligands are incorporated into each sheet.

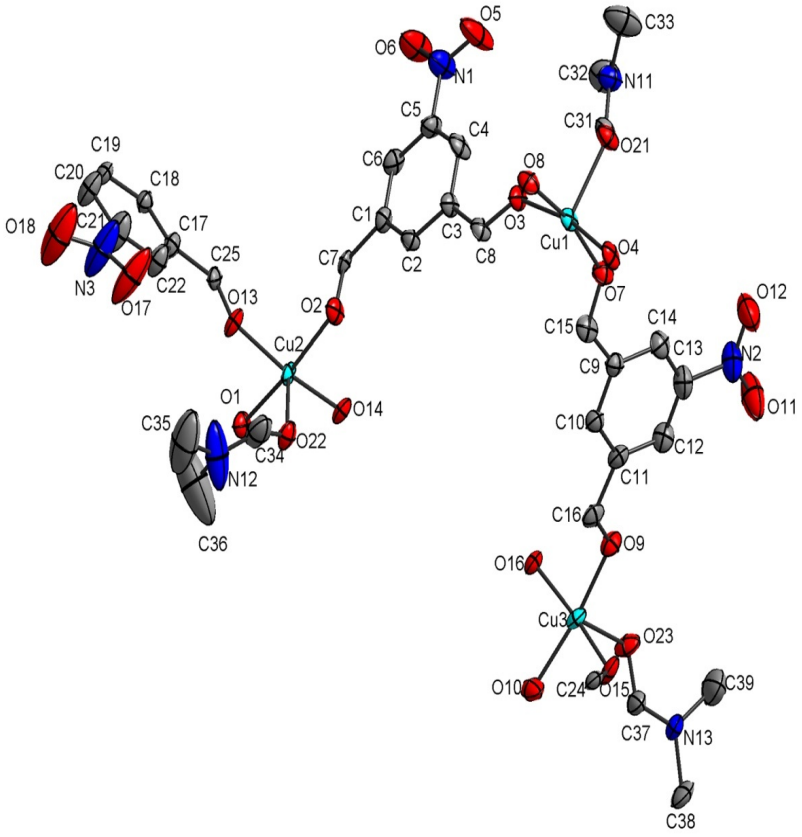

Figure 6.5 The secondary building unit(SBU) for the obtained Nitro-Cu-MOFs

The 3-Dimensional structure of Nitro-Cu-MOF complexes could be viewed via different axis in Figure 6.6, Figure 6.7 and Figure 6.8. And the crystal data and structure refinement for the obtained Nitro-Cu-MOFs could also been shown in table 6.1. The structure can be described as a 3-dimensional porous coordination polymer which consists of Cu dimers as a building unit. Each Cu atom displays 5-fold square pyramidal coordination geometry by bonding to four carboxyl oxygen and one oxygen from DMF. The X-ray crystallographic analysis revealed that 2 crystallises in the space group P-1 with 3 copper atoms, 3 5-nbdc ligands, 3 coordinated DMF molecules and 5 guest DMF molecules in the asymmetric unit, giving a formula of {[Cu_2(5-

nbdc)$_2$(DMF)$_2$] • 3/(1/3)DMF}. The material is composed of the very different SBU as the Cu-MOFs.

Due to the very different SBU structure as the Cu-MOFs, the obtained Nitro-Cu-MOFs have the potential to be very porous. The material still has the potential to be porous; however, as oval-shape d channels are present in the extended structure. These channels are 3.7 A˚ wide at the narrowest point, and in the crystal structure they are filled by guest DMF molecules.

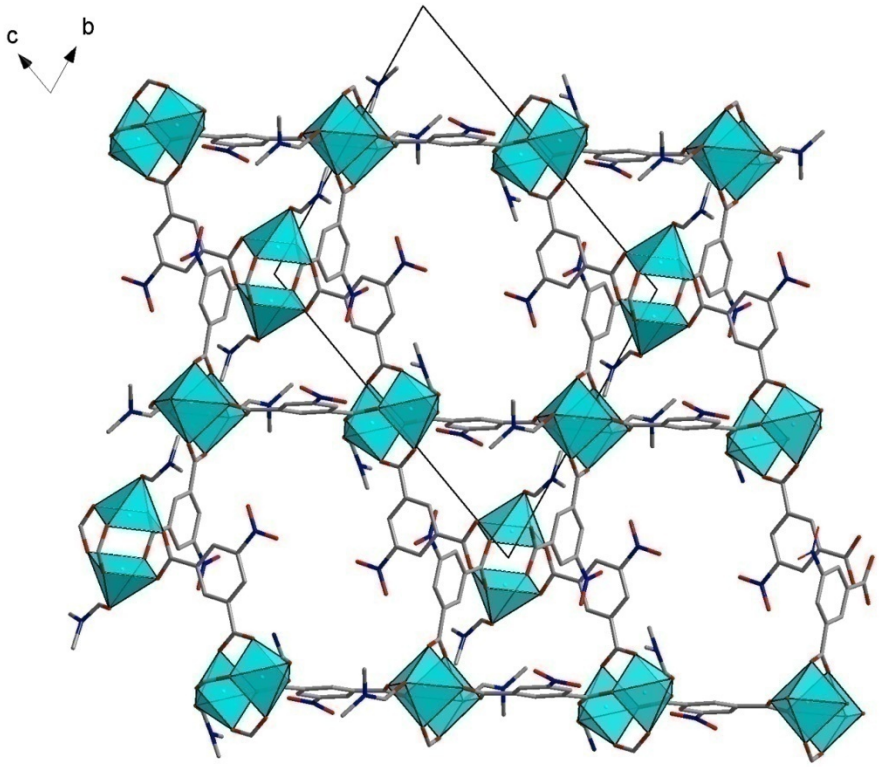

Figure 6.6 The 3-Dimensional structure for the obtained Nitro-Cu-MOFs. (View along a-axis. Hydrogen atoms are omitted for clarity)

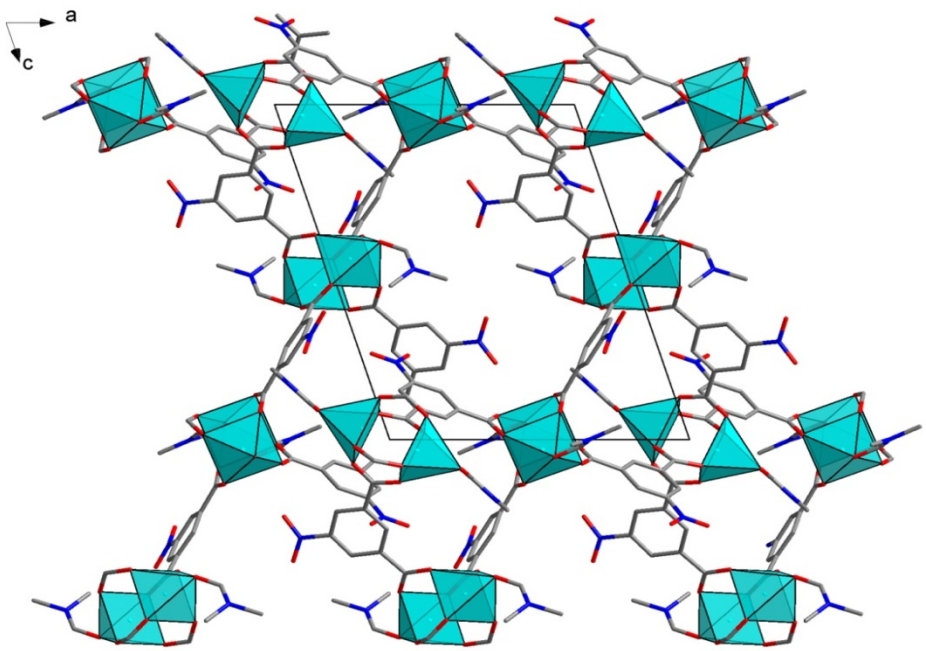

Figure 6.7 The 3-Dimensional structure for the obtained Nitro-Cu-MOFs. (View along b-axis. Hydrogen atoms are omitted for clarity)

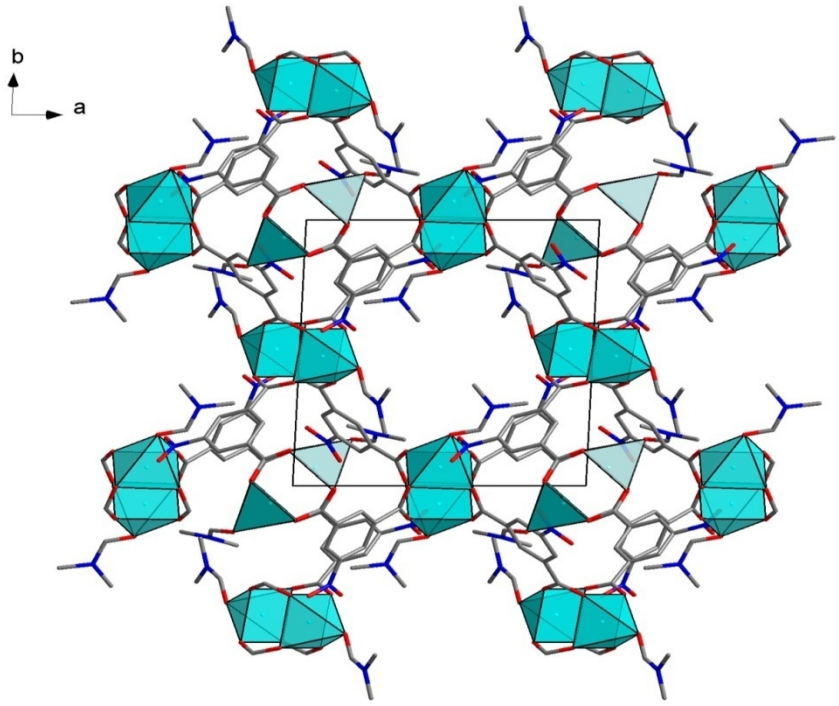

Figure 6.8 The 3-Dimensional structure for the obtained Nitro-Cu-MOFs. (View along c-axis. Hydrogen atoms are omitted for clarity)

Table 6.1 Crystal data and structure refinement for Nitro-Cu-MOFs.

Crystal data and structure refinement for the obtained Nitro-Cu-MOFs.	
Empirical formula	$C_{48}\ H_{65}\ Cu_3\ N_{11}\ O_{26}$
Formula weight	1402.73
Temperature	120 (2) K
Wavelength	0.41328 Å
Crystal system	Triclinic
Space group	P -1
Unit cell dimensions	a = 13.3142(14) Å
b = 14.6624(15) Å	β = 70.250(3)°.
c = 18.405(2) Å	γ = 80.114(2)°.
Volume	3100.1(6) $Å^3$
Z	2
Density (calculated)	1.503 Mg/m^3
Absorption coefficient	0.589 mm^{-1}
F(000)	1450
Diffractometer	Bruker APEX II
Crystal morphology & size	Blue plate, 0.10 x 0.07 x 0.04 mm^3
Theta range for data collection	0.88 to 14.42°.
Index ranges	-15<=h<=16, -17<=k<=17, -19<=l<=22
Reflections collected	47368
Independent reflections	10299 [R(int) = 0.0452]
Completeness to theta = 14.42°	90.7 %
Absorption correction	Semi-empirical from equivalents
Max. and min. transmission	0.9768 and 0.9435
Refinement method	Full-matrix least-squares on F^2
Data / restraints / parameters	10299 / 0 / 574
Goodness-of-fit on F^2	1.114
Final R indices [I>2sigma(I)]	R1 = 0.0481, wR2 = 0.1359
R indices (all data)	R1 = 0.0646, wR2 = 0.1438
Largest diff. peak and hole	0.876 and - 0.675 $e.Å^{-3}$

6.3.3 CO_2 Adsorption Results

The CO_2 adsorption curve for both Cu-MOFs and Nitro-Cu-MOFs could be shown in the Figure 6.9. It could be shown from the Figure that the excess gas uptake of the obtained Nitro-Cu-MOFs at 60 psi could be as high as 68 mg/g at 298 K for carbon dioxide, which is much higher than the performance of the Cu-MOFs (31 mg/g at 298 K for carbon dioxide).

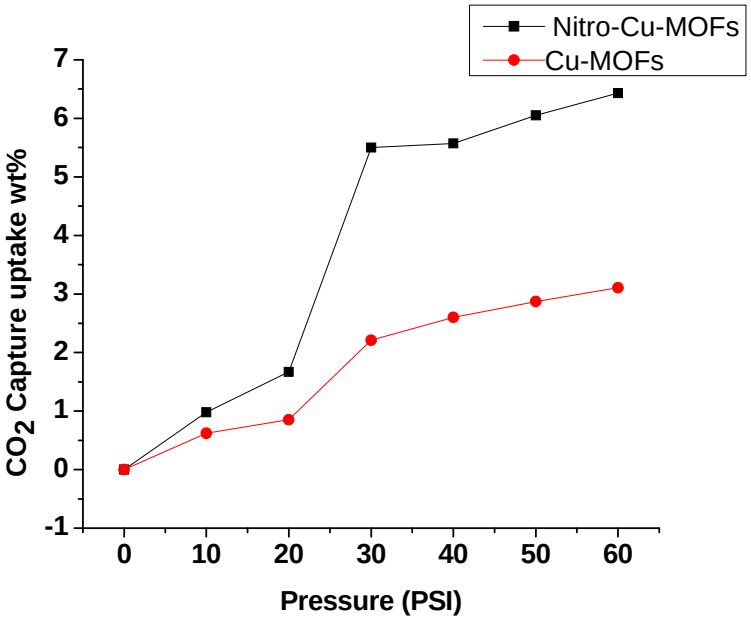

Figure 6.9 The CO_2 adsorption curve for both Cu-MOFs and Nitro-Cu-MOFs

From CO_2 uptake behavior in obtained Cu-MOFs and Nitro-Cu-MOFs materials, it is likely that the intrinsic surface area plays a critical role in determining the total capacity of gas storage. The results of structure analysis show that the obtained Nitro-Cu-MOF is composed of the very different secondary building units as the Cu-MOFs. The obtained Nitro-Cu-MOFs have the potential to be very porous due to the 3-dimensional structure, while the obtained Nitro-Cu-MOFs posses a one-dimensional polyhydroen structure. To clarify this point, the surface area and pore volume of obtained MOFs has been observed by BET. And the results have been shown in the table 6.2. The obtained

Nitro-Cu-MOFs had a specific surface area of 576.27 m^2/g and a pore volume of 0.32 m^3/g, which is much higher than obtained Cu-MOFs that had a specific surface area of 200.81 m^2/g and a pore volume of 0.30 m^3/g.

Table 6.2 Porosity measurements for Cu-MOFs and Nitro-Cu-MOFs.

Materials	Pore Size/ Å	S_{lang}/ m^2g^{-1}	S_{BET}/ m^2g^{-1}	$V_{p,DR}$/ cm^3g^{-1}
Cu-MOFs	1.5	200.81	184.23	0.30
Nitro-Cu-MOFs	2.7	576.27	467.31	0.32

6.4 Conclusion

The Nitro-Cu-MOF complexes, a new class of metal organic frameworks have been successfully synthesized via a conventional thermal reaction. Unlike the Cu-MOFs, the Nitro-Cu-MOF has a 3-dimensional structure. The obtained Nitro-Cu-MOFs had a specific surface area of 576.27 m^2/g and a pore volume of 0.32 m^3/g. The excess gas uptake of the obtained Nitro-Cu-MOFs at 60 psi could be as high as 68 mg/g at 298 K for carbon dioxide, which is much higher than the performance of the Cu-MOFs (31 mg/g at 298 K for carbon dioxide.

LIST OF REFERENCES

LIST OF REFERENCES

[1] M. Davis, "New vistas in zeolite and molecular sieve catalysis," *Accounts of Chemical Research*, vol. 26, no. 3, pp. 111-115,1993.

[2] J. Weitkamp, "Zeolites and catalysis," *Solid State Ionics*, vol. 131, no. 1-2, pp. 175-188, 2000.

[3] C. Kresge, M. Leonowicz, W. Roth, J. Vartuli and J. Beck, "Ordered mesoporous molecular sieves synthesized by a liquid-crystal template mechanism," *Nature*, vol. 359, no. 6397, pp. 710-712, 1992.

[4] R. Ryoo, C. Ko and I. Park, "Synthesis of highly ordered MCM-41 by micelle-packing control with mixed surfactants," *Chemical Communications*, vol. 1999, no. 15, pp. 1413-1414, 1999.

[5] D. Zhao, J. Feng, Q. Huo, N. Melosh, G. Fredrickson, B. Chmelka and G. Stucky, "Triblock copolymer syntheses of mesoporous silica with periodic 50 to 300 angstrom pores," *Science*, vol. 279, no. 5350, pp. 548, 1998.

[6] Y. Wei, Q. Feng, J. Xu, H. Dong, K. Qiu, S. Jansen, R. Yin and K. Ong, "Polymethacrylate-silica hybrid nanoporous materials: A bridge between inorganic and polymeric molecular sieves," *Advanced Materials*, vol. 12, no. 19, pp. 1448-1450, 2000.

[7] N. Mizuno, H. Hatayama, S. Uchida and A. Taguchi, "Tunable One-Pot syntheses of hexagonal-, cubic-, and lamellar-Mesostructured vanadium-phosphorus oxides," *Chem. Mater*, vol. 13, no. 1, pp. 179-184, 2001.

[8] Y. Yao, M. Zhang, J. Shi, M. Gong, H. Zhang and Y. Yang, "Encapsulation of fluorescein into MCM-41 mesoporous molecular sieve by a sol-gel method," *Materials Letters*, vol. 48, no. 1, pp. 44-48, 2001.

[9] Z. Sun, L. Liu, L. Zhang and D. Jia, "Rapid synthesis of ZnO nano-rods by one-step, room-temperature, solid-state reaction and their gas-sensing properties," *Nanotechnology*, vol. 17, pp. 2266-2270, 2006.

[10] L. Qingwen, W. Yiming and L. Guoan, "pH-Response of nanosized MnO2 prepared with solid state reaction route at room temperature," *Sensors and Actuators B: Chemical*, vol. 59, no. 1, pp. 42-47, 1999.

[11] J. Goodenough, A. Padhi, K. Nanjundaswamy and C. Masquelier, "Cathode materials for secondary (rechargeable) lithium batteries," *Journal of Power Sources*, vol. 174, no. 2, pp. 154-168, 1999.

[12] S. Chung, J. Bloking and Y. Chiang, "Electronically conductive phospho-olivines as lithium storage electrodes," *Nature materials*, vol. 1, no. 2, pp. 123-128, 2002.

[13] N. Meethong, Y. Kao, M. Tang, H. Huang, W. Carter and Y. Chiang, "Electrochemically induced phase transformation in nanoscale olivines Li_{1-x} MPO_4 (M = Fe, Mn)," *Journal of Chemical Materials,* vol. 20, no. 19, pp. 6189–6198, 2008.

[14] T. Drezen, N. Kwon, P. Bowen, I. Teerlinck, M. Isono and I. Exnar, "Effect of particle size on $LiMnPO_4$ cathodes," *Journal of Power Sources*, vol. 174, no. 2, pp. 949-953, 2007.

[15] N. Bramnik and H. Ehrenberg, "Precursor-based synthesis and electrochemical performance of $LiMnPO_4$," *Journal of Alloys and Compounds*, vol. 464, no. 1-2, pp. 259-264, 2008.

[16] M. Gruss and R. Glaum, "Refinement of the superstructure of C-Type chromium (III) Tris (metaphosphate), $Cr(PO_3)_3$," *Acta Crystallographica Section C: Crystal Structure Communications*, vol. 52, no. 11, pp. 2647-2650, 1996.

[17] A. Schmidt, R. Glaum and J. Beck, "Preparation and crystal structure of $Cr_4(Si_2O_7)X_2$ (X= Cl, Br): The First Chromous Halide-Disilicates," *Journal of Solid State Chemistry*, vol. 127, no. 2, pp. 331-340, 1996.

[18] S. Mustafa, S. Murtaza, A. Naeem and K. Farina, "Sorption of divalent metal ions on $CrPO_4$," *Journal of colloid and interface science*, vol. 283, no. 2, pp. 287-293, 2005.

[19] S. Mustafa, S. Murtaza, A. Naeem and K. Farina, "Ion exchange sorption of Pb^{2+} ions on $CrPO_4$," *Environmental technology*, vol. 26, no. 4, pp. 353-360, 2005.

[20] S. Zhang, J. Allen, K. Xu and T. Jow, "Optimization of reaction condition for solid-state synthesis of $LiFePO_4$-C composite cathodes," *Journal of Power Sources*, vol. 147, no. 1-2, pp. 234-240, 2005.

[21] S. Franger, F. Le Cras, C. Bourbon and H. Rouault, "Comparison between different $LiFePO_4$ synthesis routes and their influence on its physico-chemical properties," *Journal of Power Sources*, vol. 119, pp. 252-257, 2003.

[22] F. Zhou, K. Kang, T. Maxisch, G. Ceder and D. Morgan, "The electronic structure and band gap of $LiFePO_4$ and $LiMnPO_4$," *Solid State Communications*, vol. 132, no. 3-4, pp. 181-186, 2004.

[23] C. Xing, L. Peng, W. Zhang and Y. He, "Synthesis and performance of $LiMnPO_4$ used as cathode material for lithium ion batteries [J]," *Acta Physico-chimica Sinica*, vol. 10, pp. 64-71, 2004.

[24] H. Fang, Y. Yang, G. Yan and G. Li, "Carbonate anions controlled morphological evolution of $LiMnPO_4$ crystals," *Chemical Communications*, vol. 2008, no. 9, pp. 1118-1120, 2008.

[25] N. Stock, G. Ferey and A. Cheetham, "Hydrothermal synthesis and characterization of a chromium (II) pyrophosphate, $Na_2CrP_2O_7 \cdot 0.5\ H_2O$," *Solid State Sciences*, vol. 2, no. 2, pp. 307-312, 2000.

[26] A. Tarafdar, S. Biswas, N. Pramanik and P. Pramanik, "Synthesis of mesoporous chromium phosphate through an unconventional sol-gel route," *Microporous and Mesoporous Materials*, vol. 89, no. 1-3, pp. 204-208, 2006.

[27] F. Bautista, J. Campelo, A. Garcia, D. Luna, J. Marinas and M. Urbano, "Effect of precipitation medium and thermal treatment on structure and textural properties of chromium orthophosphates," *Reaction Kinetics and Catalysis Letters*, vol. 49, no. 1, pp. 173-181, 1993.

[28] R. Ravikumar, J. Yamauchi, A. Chandrasekhar, Y. Reddy and P. Rao, "Identification of chromium and nickel sites in zinc phosphate glasses," *Journal of Molecular Structure*, vol. 740, no. 1-3, pp. 169-173, 2005.

[29] L. Liu, H. Li and Y. Zhang, "Effect of synthesis parameters on the chromium content and catalytic activities of mesoporous Cr-MSU-x prepared under acidic conditions," Journal of Physical Chemistry B, vol. 110, no. 31, pp. 15478-15485, 2006.

[30] L. Frunza, J. Pelgrims, H. Leeman, P. Van Der Voort, E. Vansant, R. Schoonheydt and B. Weckhuysen, "Incorporation of transition metal ions in aluminophosphate molecular sieves with AST structure," *Journal of Physical Chemistry B*, vol. 105, no. 14, pp. 2677-2686, 2001.

[31] A. Beale, D. Grandjean, J. Kornatowski, P. Glatzel, F. de Groot and B. Weckhuysen, "Unusual coordination behavior of Cr^{3+} in microporous aluminophosphates," *Journal of Physical Chemistry B*, vol. 110, no. 2, pp. 716-722, 2006.

[32] S. Laha and R. Gläser, "Characterization and catalytic performance of [Cr]MCM-41 and [Cr]MCM-48 prepared by either classical or microwave heating," *Microporous and Mesoporous Materials*, vol. 99, no. 1-2, pp. 159-166, 2007.

[33] C. Subrahmanyam, B. Louis, F. Rainone, B. Viswanathan, A Renken and T. Varadarajan, "Catalytic oxidation of toluene with molecular oxygen over Cr-substituted mesoporous materials," *Applied Catalysis A: General*, vol. 241, no. 1-2, pp. 205-215, 2003.

[34] B. Weckhuysen, I. Wachs and R. Schoonheydt, "Surface chemistry and spectroscopy of chromium in inorganic oxides," *Chemical Reviews*, vol. 96, no. 8, pp. 3327-3350, 1996.

[35] R. Sheldon, "Selective catalytic synthesis of fine chemicals: opportunities and trends," *Journal of Molecular Catalysis A: Chemical*, vol. 107, no. 1-3, pp. 75-83, 1996.

[36] F. Bautista, J. Campelo, A. Garcia, D. Luna, J. Marinas, A. Romero and M. Urbano, "Conversion of 2-propanol over chromium orthophosphates," *Reaction Kinetics and Catalysis Letters*, vol. 55, no. 1, pp. 133-141, 1995.

[37] R. Signorell, M. Jetzki, M. Kunzmann and R. Ueberschaer, "Unraveling the origin of band shapes in infrared spectra of N_2O-$12CO_2$ and $12CO_2$-$13CO_2$ ice particles," *Journal of Physical Chemistry A*, vol. 110, no. 9, pp. 2890-2897, 2006.

[38] A. Yuan, J. Wu, L. Bai, S. Ma, Z. Huang and Z. Tong, "Standard molar enthalpies of formation for ammonium/3d-Transition metal phosphates $NH_4MPO_4 \cdot H_2O$ (M= Mn^{2+}, Co^{2+}, Ni^{2+}, Cu^{2+})," *Journal of Chemical Engineering*, vol. 53, no. 5, pp. 1066-1070, 2008.

[39] F. Bautista, J. Campelo, A. Garcia, D. Luna, J. Marinas, A. Romero and M. Urbano, "Chromium-aluminium orthophosphates, III. Acidity and catalytic performance in cyclohexene and cumene conversions on $CrPO_4$-$AlPO_4$ (20–50 wt.% $AlPO_4$) catalysts obtained in aqueous ammonia," *Reaction Kinetics and Catalysis Letters*, vol. 53, no. 1, pp. 55-63, 1994.

[40] A. Monnier, F. Schuth, Q. Huo, D. Kumar, D. Margolese, R. Maxwell, G. Stucky, M. Krishnamurty, P. Petroff and A. Firouzi, "Cooperative formation of inorganic-organic interfaces in the synthesis of silicate mesostructures," *Science*, vol. 261, no. 5126, pp. 1299, 1993.

[41] S.M. Benson and T. Surles, "Carbon dioxide capture and storage: An overview with emphasis on capture and storage in deep geological formations," *Proceedings of the Ieee*, vol. 94, no. 10, pp. 1795-1805, 2006.

[42] S. Bode, "Carbon dioxide capture and storage under the clean development mechanism: opportunities and risks," *Gaia-Ecological Perspectives for Science and Society*, vol. 18, no. 4, pp. 300-306, 2009.

[43] R. Grunwald, "A review of carbon dioxide capture and storage - technology, potentials, risks, costs, and regulation," *Gaia-Ecological Perspectives for Science and Society*, vol. 18, no. 3, pp. 211-220, 2009.

[44] S. Murai and Y. Fujioka, "Challenges to the carbon dioxide capture and storage (CCS) technology," *Ieej Transactions on Electrical and Electronic Engineering*, vol. 3, no. 1, pp. 37-42, 2008.

[45] D.J. Tranchemontagne, J.L. Mendoza-Cortes, M. O'Keeffe and O.M. Yaghi, "Secondary building units, nets and bonding in the chemistry of metal-organic frameworks," *Chemical Society Reviews*, vol. 38, no. 5, pp. 1257-1283, 2009.

[46] A.U. Czaja, N. Trukhan and U. Muller, "Industrial applications of metal-organic frameworks," *Chemical Society Reviews*, vol. 38, no. 5, pp. 1284-1293, 2009.

[47] R. Banerjee, H. Furukawa, D. Britt, C. Knobler, M. O'Keeffe and O.M. Yaghi, "Control of pore size and functionality in isoreticular zeolitic imidazolate frameworks and their carbon dioxide selective capture properties," *Journal of the American Chemical Society*, vol. 131, no. 11, pp. 3875-3876, 2009.

[48] R. Banerjee, A. Phan, B. Wang, C. Knobler, H. Furukawa, M. O'Keeffe and O.M. Yaghi, "High-Throughput synthesis of zeolitic imidazolate trameworks and application to CO_2 capture," *Science*, vol. 319, no. 5865, pp. 939-943, 2008.

[49] D. Britt, H. Furukawa, B. Wang, T.G. Glover and O.M. Yaghi, "Highly efficient separation of carbon dioxide by a metal-organic framework replete with open metal sites," *Proceedings of the National Academy of Sciences of the United States of America*, vol. 19, no. 165, pp. 639-643, 2009.

[50] B. Wang, A.P. Cote, H. Furukawa, M. O/'Keeffe and O.M. Yaghi, "Colossal cages in zeolitic imidazolate frameworks as selective carbon dioxide reservoirs," *Nature*, vol. 453, no. 7192, pp. 207-211, 2008.

[51] M. Eddaoudi, J. Kim, J.B. Wachter, H.K. Chae, M. O'Keeffe and O.M. Yaghi, "Porous metal-organic polyhedra: 25 angstrom cuboctahedron constructed from 12 Cu-2(CO_2)(4) paddle-wheel building blocks," *Journal of the American Chemical Society*, vol. 123, no. 18, pp. 4368-4369, 2001.